

Monochromatic Pc5 Modulations of the Ionospheric Velocities and TEC and GOES-16 Magnetic Field Associated with Repeated Solar Wind Dynamic Pressure Enhancement

Ram Singh¹, Young-Sook Lee², and Yong Ha Kim²

¹Dept. of Astronomy and Space Science, College of Natural Sciences, Chungnam National University Daejeon, South Korea

²Chungnam National University

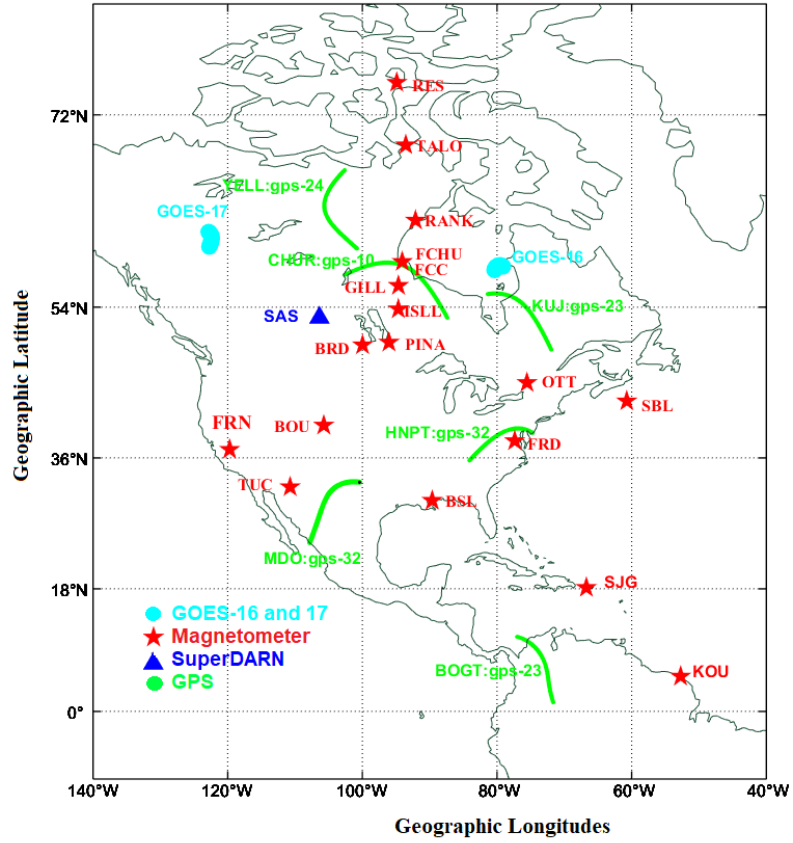
April 16, 2023

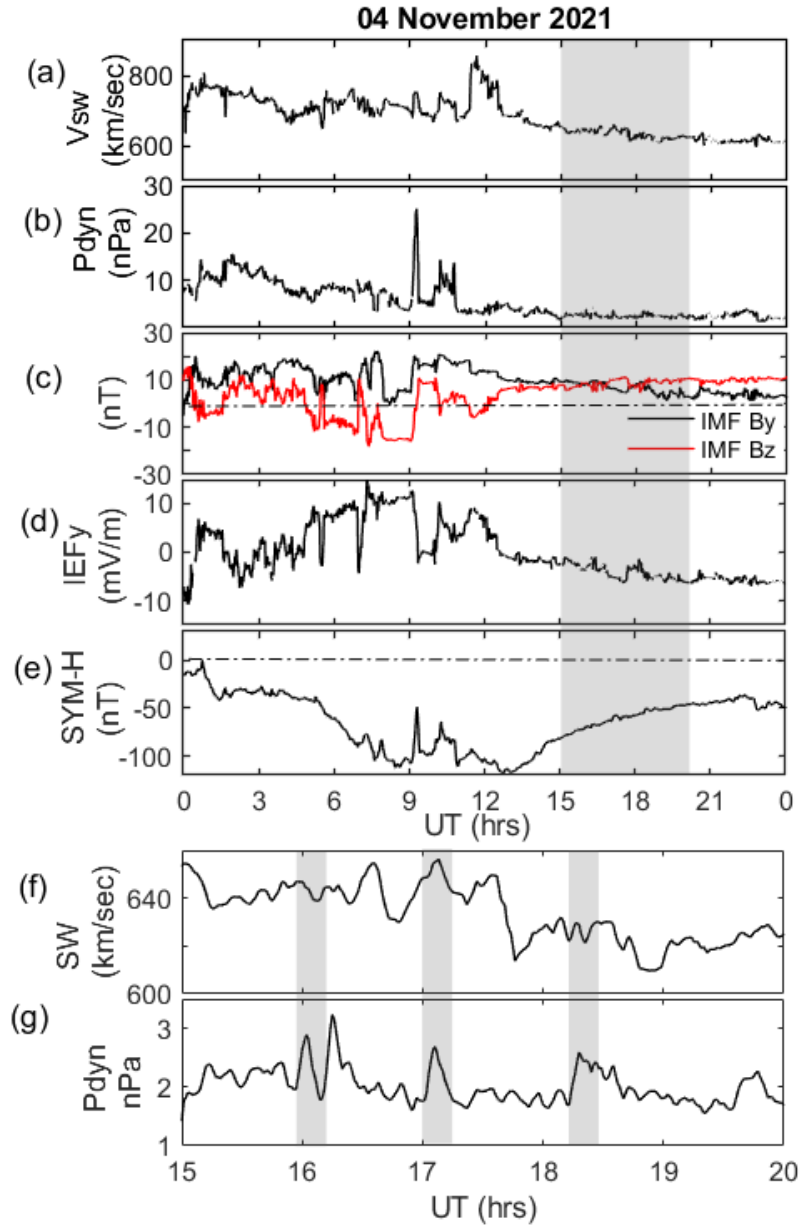
Abstract

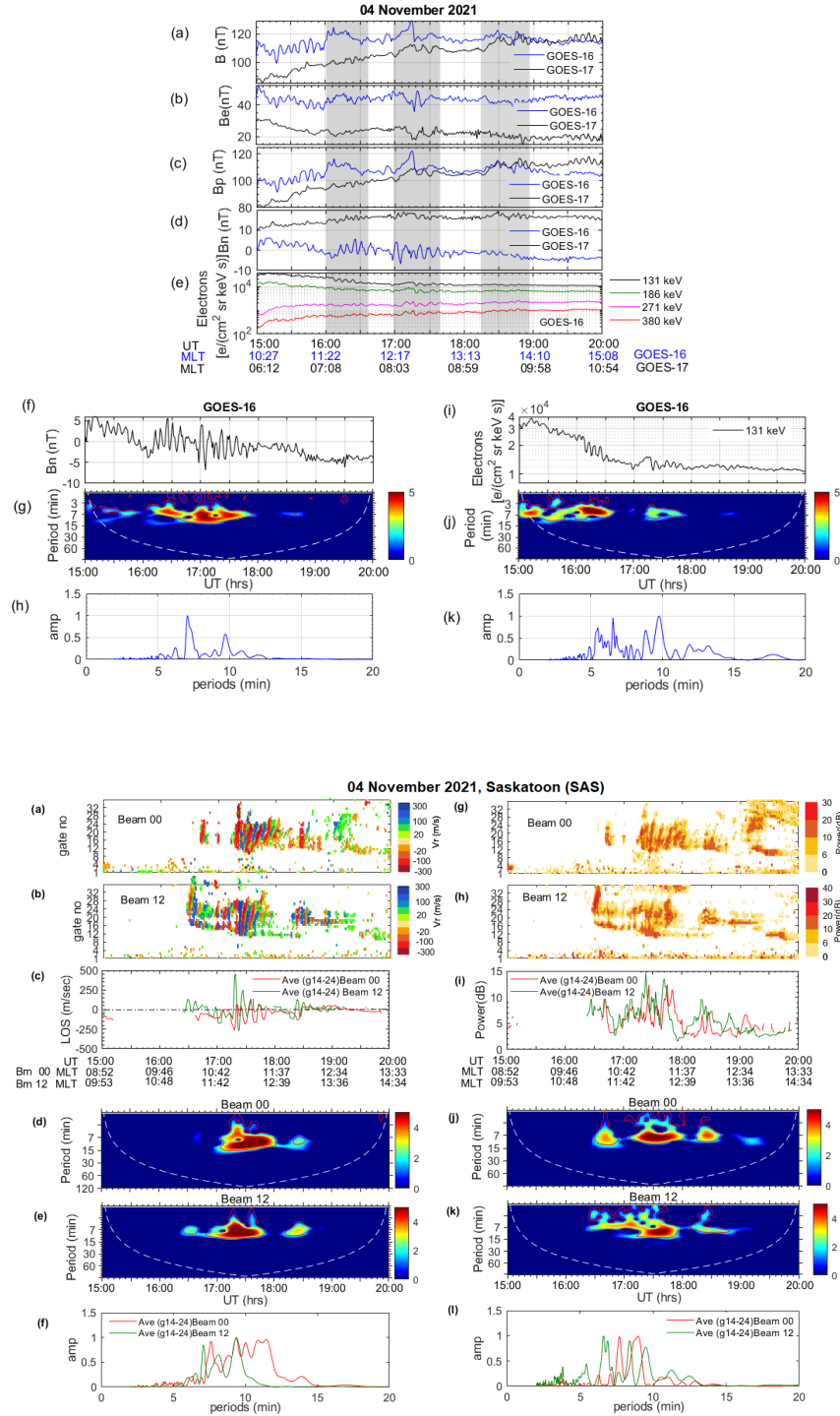
This study presents ultra-low frequency (ULF) Pc5 discrete spectrum simultaneously observed in the magnetosphere and high- to low-latitude ionospheres near noon hours (~10-14 MLT) during the recovery phase of geomagnetic storm on November 4, 2021. During the recovery phase, magnetospheric toroidal mode oscillations (GOES-16 Bn) appeared according to solar wind dynamic pressure enhancements after GOES Bp and Be (poloidal mode) oscillations precede during high solar wind speeds. When Bn oscillates, the ionospheric line-of-sight (LOS) velocity and echo power oscillate at the same discrete frequencies of 1.7 and 2.2 mHz (9.7 and 7.5 min), observed by Super Dual Auroral Radar Network (SuperDARN) at Saskatoon (eastward LOS). The period of negative LOS velocity (away from the radar) for 7.5 min or 9.7 min corresponds to echo power increase. This signifies that both the ionospheric density and poleward convection velocity increase are driven by the periodic forcing of the convection electric field and energetic electron precipitation. The same frequency pulsations have also been observed in the geomagnetic field (H-component) and Global Positioning System (GPS) total electron content (TEC) from high- to low-latitude ionosphere. The oscillation frequency of the H-component is consistently preserved at 1.7 mHz (9.7 min) down to low latitudes. The Pc5 oscillations at high to low latitudes can be attributed to toroidal mode Alfvén waves and the compressional mode propagating across magnetic field lines as well as the fast magnetosonic waveguide mode at work by the solar wind dynamic pressure enhancements at high solar wind speeds.

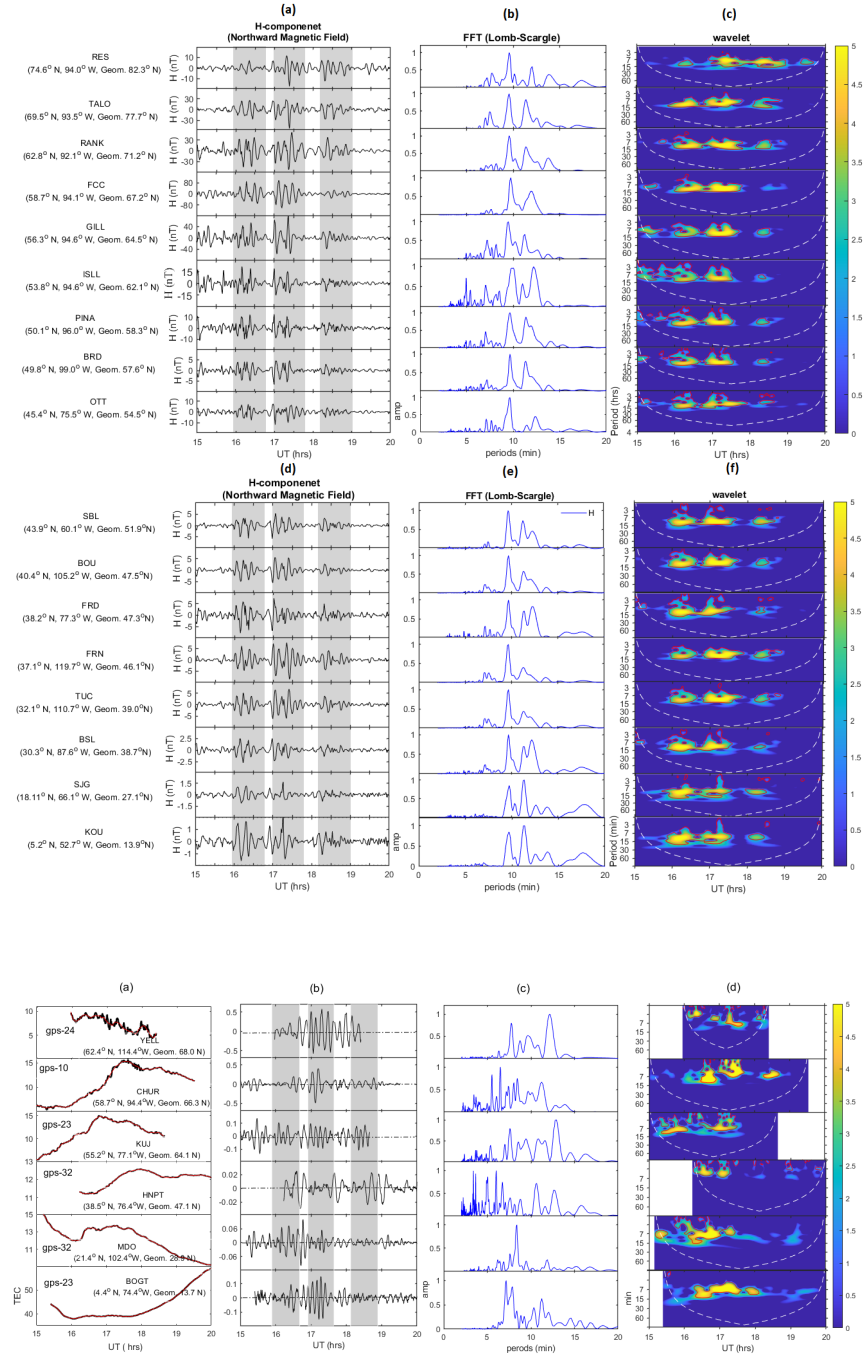
Hosted file

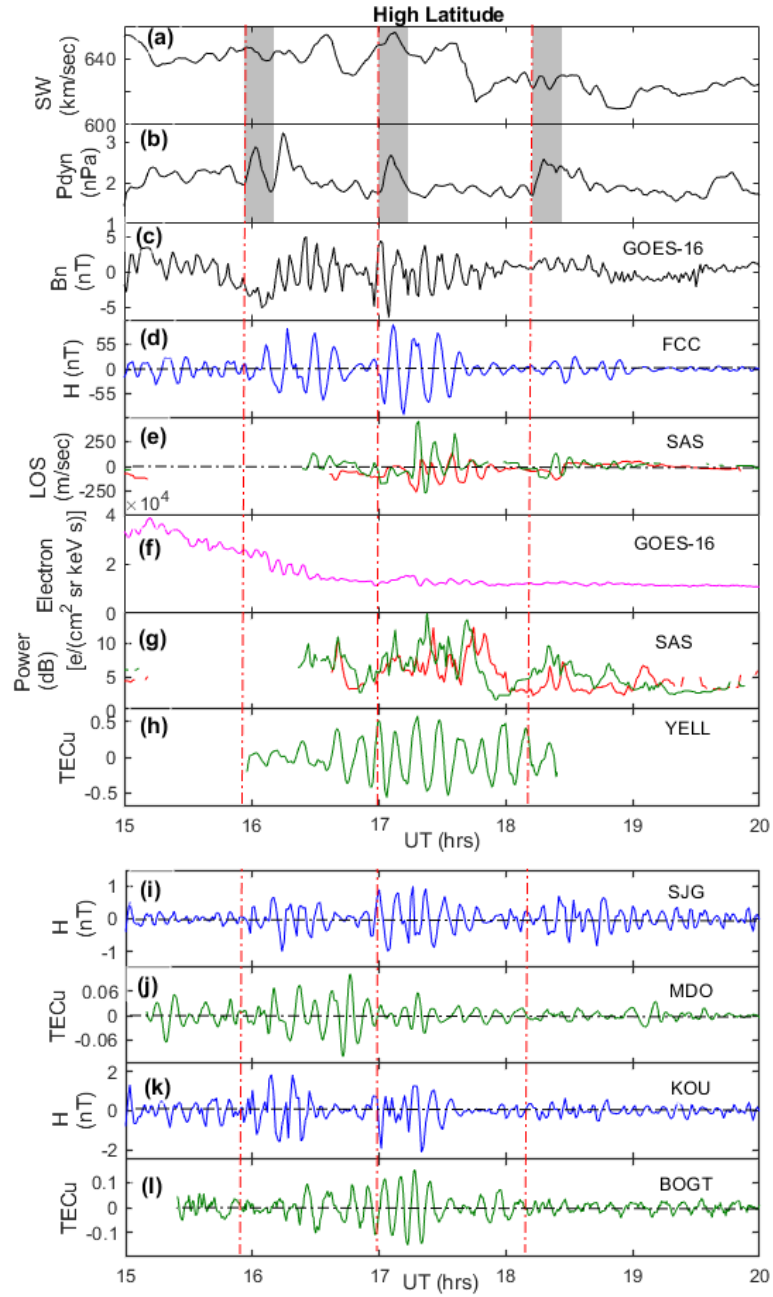
960447_0_art_file_10870813_rs3wcp.docx available at <https://authorea.com/users/558291/articles/634328-monochromatic-pc5-modulations-of-the-ionospheric-velocities-and-tec-and-goes-16-magnetic-field-associated-with-repeated-solar-wind-dynamic-pressure-enhancement>











1 **Monochromatic Pc5 Modulations of the Ionospheric Velocities and TEC and GOES-16**
2 **Magnetic Field Associated with Repeated Solar Wind Dynamic Pressure Enhancement**

3
4 Ram Singh, Young-Sook Lee, and Yong Ha Kim

5
6 Department of Astronomy and Space Science, Chungnam National University, Daejeon,
7 South Korea

8
9 Corresponding author: Ram Singh (email:ramphysics4@gmail.com)

10
11 **Key points**

- 12 1) Simultaneous observations of ultra-low frequency (ULF) Pc5 oscillations in the
13 magnetosphere and high to low-latitude ionosphere
- 14 2) Dominant Pc5 discrete frequency (1.7 mHz) retained consistently without significant
15 changes
- 16 3) A series of three monochromatic oscillations observed in the magnetosphere and
17 ionosphere

18
19 **Abstract**

20 This study presents ultra-low frequency (ULF) Pc5 discrete spectrum simultaneously
21 observed in the magnetosphere and high- to low-latitude ionospheres near noon hours (~10-
22 14 MLT) during the recovery phase of geomagnetic storm on November 4, 2021. During the
23 recovery phase, magnetospheric toroidal mode oscillations (GOES-16 Bn) appeared
24 according to solar wind dynamic pressure enhancements after GOES Bp and Be (poloidal
25 mode) oscillations precede during high solar wind speeds. When Bn oscillates, the
26 ionospheric line-of-sight (LOS) velocity and echo power oscillate at the same discrete
27 frequencies of 1.7 and 2.2 mHz (9.7 and 7.5 min), observed by Super Dual Auroral Radar
28 Network (SuperDARN) at Saskatoon (eastward LOS). The period of negative LOS velocity
29 (away from the radar) for 7.5 min or 9.7 min corresponds to echo power increase. This
30 signifies that both the ionospheric density and poleward convection velocity increase are

31 driven by the periodic forcing of the convection electric field and energetic electron
32 precipitation. The same frequency pulsations have also been observed in the geomagnetic
33 field (H-component) and Global Positioning System (GPS) total electron content (TEC) from
34 high- to low-latitude ionosphere. The oscillation frequency of the H-component is
35 consistently preserved at 1.7 mHz (9.7 min) down to low latitudes. The Pc5 oscillations at
36 high to low latitudes can be attributed to toroidal mode Alfvén waves and the compressional
37 mode propagating across magnetic field lines as well as the fast magnetosonic waveguide
38 mode at work by the solar wind dynamic pressure enhancements at high solar wind speeds.

39 **Plain Language Summary**

40 Pc5 ultra-low frequency (ULF) oscillations in the Earth's magnetosphere play an important
41 role in the transfer of energy in the magnetosphere and ionosphere, including solar wind
42 magnetosphere interaction, and coupling with different plasma wave modes and plasma
43 instabilities. This study presents simultaneous observations of Pc5 wave oscillations in the
44 magnetosphere and high to low-latitude ionosphere near noon hours. Three times increase in
45 solar wind dynamic pressure prompted the occurrence of three monochromatic oscillation
46 packets in Bn, high-to-low latitude ground north-south magnetic field (H), SuperDARN LOS
47 velocity and echo power, and GPS TEC (high-low latitudes). The azimuthal eastward
48 component of the magnetic field (poloidal mode (Bn)) and electron flux intensities showed
49 oscillations in the Pc5 discrete spectrum with dominant periodicities of 7.5 and 9.7 min (2.2
50 and 1.7 mHz) in the magnetosphere. The dominant Pc5 discrete frequencies occurring in the
51 magnetosphere and at high latitudes are consistently preserved all the way to low latitudes
52 without significant changes. Magnetic field oscillations active in toroidal field line
53 resonances in the magnetosphere affect oscillations in ionospheric velocity, plasma density,
54 and ground magnetic field at high latitudes.

55 **Keywords**

56 Magnetosphere, ionosphere, Pc5 pulsations, SuperDARN, GPS-TEC, Magnetometer.

57 **1. Introduction**

58 Pc5 ultra-low frequency (ULF, 1.6-6.7 mHz) waves can be used to diagnose several
59 magnetospheric properties, such as the acceleration of auroral electrons, particle scattering,
60 and energization and transport of radiation belt electrons (Samson et al., 1992a; Elkington et
61 al., 1999), as well as ground phenomena, such as geomagnetically induced currents which

62 can cause damage to technological infrastructure (Belakhovsky et al., 2019; Boteler et al.,
63 1998; Yagova et al., 2021). The ULF perturbations in the magnetosphere can be caused by a
64 variety of external (e.g., by the solar wind) or internal (e.g., by the resonance with energetic
65 particles) sources. The external drivers of ULF waves in the magnetosphere include the
66 Kelvin-Helmholtz Instability (KHI) via surface waves, direct solar wind pressure changes,
67 and solar wind discontinuation (Chen & Hasegawa, 1974; Southwood, 1974; Allan et al.,
68 1986; Wright and Rickard, 1995; Mann et al., 1999). The ULF waves detected on the ground
69 are not always the same as those entering the magnetosphere via the solar wind. As waves
70 generated outside the magnetosphere must pass through the magnetopause, wave energy is
71 transformed and amplified by processes occurring within the magnetosphere, such as field
72 line resonance (FLR) and other cavity resonances (Samson et al., 1991; Kivelson et al.,
73 1984; Kivelson and Southwood, 1986; Southwood and Kivelson, 1990).

74 Previous studies have reported pressure pulse-induced FLR at different discrete frequencies
75 of 1.3, 1.9, 2.6, and 3.3 mHz in the Pc5 spectrum which occurred simultaneously at different
76 latitudes (Samson et al., 1991; Ruohoniemi et al., 1991; Walker et al., 1992; Baddeley et
77 al.2007). Baddeley et al. (2007) examined the latitudinal and longitudinal characteristics of
78 Pc5 pulsations with dominant frequencies of 1.7, 2.6, 3.3, 4.2, and 5.4 mHz in the dawn flank
79 induced by a sudden increase in solar wind dynamic pressure.

80 Pc5 wave pulsations can significantly modulate ionospheric and magnetospheric parameters
81 including the electric field, plasma convection velocity, field-aligned current, precipitating
82 electron flux, ionosphere conductance, electron and ion temperatures, and total electron
83 content (TEC) (Lester et al., 2000; Ponomarenko et al., 2001; Sakaguchi et al., 2012;
84 Norouzi-Sedeh et al., 2015; Belakhovsky et al., 2016; Fenrich et al., 2019; Kozyreva et al.,
85 2020). Modern ground-based sounding techniques, such as HF Doppler sounders,
86 SuperDARN radars, trans ionospheric radio wave propagation, and riometers, can detect local
87 variations in ionospheric electron density caused by long-period ULF waves (Fenrich et
88 al., 1995; Ziesolleck et al., 1998; Ponomarenko et al., 2001; Pilipenko et al. 2014a; Watson et
89 al.,2015; Vorontsova et al, 2016; Fenrich et al., 2019; Kozyreva et al., 2020). The GPS-TEC
90 technique can also detect certain types of ULF waves in the ionosphere including the Pc5
91 waves at high latitudes and Pc3-4/Pi2 waves at mid latitudes (Davies & Hartman, 1976;
92 Hamada et al., 2015). The mechanism of TEC modulation by ULF waves is still unknown
93 and challenging for the MHD wave theory. According to Skone and Nicholsons (2006), the

94 relative disturbance of the TEC caused by Pc3 waves compared to quiet times is similar to or
95 even larger than that of the geomagnetic field. At high latitudes, the relative amplitude of
96 TEC variation is larger than that of geomagnetic pulsations (Pilipenko et al., 2014a).

97 Previous studies have shown that the latitudinal structure and azimuthal propagation
98 characteristics of ULF waves can be examined very effectively by using ground
99 magnetometers and the Super Dual Auroral Radar Network (SuperDARN) (Ziesolleck et al.,
100 1998; Ponomarenko et al., 2001; Pilipenko et al. 2014a; Watson et al., 2015; Fenrich et al.,
101 2019; Kozyreva et al., 2020). Kozyreva et al. (2020) showed simultaneous modulations in
102 SuperDARN Doppler velocity, GPS TEC, and ground magnetometer data by ULF waves.
103 They suggested that a sudden increase in solar wind density triggers transient Pc5 pulsations
104 on the morning flank of the magnetosphere in both the geomagnetic field and ionospheric
105 plasma. Pilipenko et al. (2014a) and Watson et al. (2015) demonstrated the ULF waves
106 induced modulations in the ionospheric plasma using ground-based TEC measurements.
107 Baddeley et al. (2007) reported Pc5 wave characteristics in the dawn and dusk flanks. They
108 hypothesized that an abrupt rise in solar wind dynamic pressure could induce a Kelvin-
109 Helmholtz-driven waveguide mode, which would cause a large increase in wave activity and
110 FLR structures.

111 The occurrence of Pc5 pulsations at low and equatorial latitudes has been explained in
112 numerous studies using a variety of processes (Ziesolleck and Chamalaun 1993; Reddy et al.
113 1994; Shinohara et al., 1998; Motoba et al. 2002; Huang 2021). Ziesolleck and Chamalaun
114 (1993) suggested that the spatial characteristics of Pc5 pulsations at low latitudes are
115 consistent with the magnetic ground signatures of global compressional modes or large-scale
116 cavity resonances. Reddy et al. (1993) and Motoba et al. (2002) proposed that in contrast to
117 the effects of directly incoming hydromagnetic waves on the low-latitude ionosphere, electric
118 field oscillations at low and equatorial latitudes were caused by $E \times B$ effects due to
119 ionospheric electric field penetration from high latitudes to the equator.

120 In this study, we present observations of monochromatic Pc5 oscillations in the
121 magnetosphere and high- to low-latitude ionospheres driven by repeated solar wind dynamic
122 pressure enhancements at high solar wind speeds during the recovery phase of strong
123 magnetic storms on November 4, 2021. It is evident that dominant Pc5 discrete frequencies
124 occurring in the magnetosphere and high latitudes are consistently preserved all the way to
125 low latitudes without significant changes. This paper is structured as follows: Section 2

126 outlines the data source analyzed. Section 3 presents the observations and results. The
127 interplanetary and geomagnetic conditions are presented in Section 3.1. Geosynchronous,
128 particle and magnetic field observations (GOES-16 and GOES-17) and ground-based and
129 ionospheric measurements (SuperDARN/Magnetometer/GPS TEC) are presented in sections
130 3.2 and 3.3. Sections 4 and 5 contain the discussion and conclusion, respectively.

131

132 **2. Observational information and data sets**

133 We used datasets obtained from the American longitudinal region. The solar wind and
134 geomagnetic condition data at 1-minute cadence were obtained from CDAWEB
135 (<http://cdaeb.gsfc.nasa.gov>), measured by the Advanced Composition Explorer (ACE)
136 satellite, which monitors the interplanetary medium conditions near the L1 point. Ground-
137 based magnetic field data were obtained from the SuperMAG magnetometer network
138 (<http://supermag.jhuapl.edu>) and the Canadian Array for Real-time Investigations of
139 Magnetic Activity (CARISMA) (<https://www.carisma.ca/carisma>), and their site locations are
140 shown in Figure 1. The space-based geomagnetic field data and energetic electron fluxes
141 were analyzed from the fluxgate magnetometer and energetic particle sensor mounted on
142 GOES-16 and GOES-17, respectively. The satellite footprints GOES-16 (Geog./Geom.):
143 58.2°N, 79.4°W/67.68°N, 9.8°W; and GOES-17 (Geog./Geom.): 61.5°N, 123.7°W/66.3°N,
144 67.6°W) are indicated in Figure 1. The GOES-16/-17 magnetic field components and electron
145 flux data at 1 min cadence were obtained from [https://www.ngdc.noaa.gov/stp/satellite/goes-](https://www.ngdc.noaa.gov/stp/satellite/goes-r.html)
146 [r.html](https://www.ngdc.noaa.gov/stp/satellite/goes-r.html). We examined the HF SuperDARN radar data from Saskatoon (Geog: 52.1°N,
147 106.6°W, Geom: 60.8°N, 40.8°W), which is set up for the eastward field of view and reserved
148 for the observation of the high-latitude ionosphere. SuperDARN data can be downloaded
149 from the site <https://ergsc.isee.nagoya-u.ac.jp/>, a ground measurement repository created for
150 the About Exploration of energization and Radiation in Geospace "ARASE" (ERG) mission.
151 The SuperDARN radar has a field of view with 15 beams in azimuth and 75 range gates with
152 a width of 45 km, starting at a distance of 180 km distance in the extension of the oblique
153 geometry. GPS TEC data with a 30 s resolution from an array of GPS receivers in American
154 longitudes were taken from <ftp://cddis.gsfc.nasa.gov/pub/gps/data>, and the site location is
155 shown in Figure 1.

156 **3. Observational Results**

157 In this section, we present the discrete frequency spectra in the ULF Pc5 band detected in
158 various datasets obtained for the magnetospheric and ionospheric (high- to low-latitudes)
159 observations during the recovery phase of the magnetic storm on November 4, 2021.

160 **3.1 Interplanetary magnetic field and geomagnetic conditions**

161 The main effects of solar wind and interplanetary magnetic field on Earth's magnetosphere
162 and ionosphere are demonstrated here. To specify time intervals for the analysis, the solar
163 wind and geomagnetic conditions for November 4, 2021, are presented in Figure 2. Figure 2
164 shows, from top to bottom, the (a) change in solar wind velocity (V_{sw}), (b) solar wind
165 dynamic pressure (P_{dyn}), (c) y- and z-components of the interplanetary magnetic field (IMF:
166 B_y and B_z in black and red); (d) the interplanetary electric field (IEF E_y) calculated from E_y
167 $= -V_{sw} \times B_z$, (e) Sym-H, and (f-g) an enlarged view of V_{sw} and P_{dyn} between 1500-2000
168 UT. The time interval from 1500-2000 UT is indicated with a grey shade because discrete
169 frequencies of the Pc5 wave band occurred simultaneously in the magnetosphere and
170 ionosphere. The geomagnetic storm that started from 23 UT on November 3, 2021, is
171 considered to be recovering at ~ 1300 UT with SYM-H of -120 nT. During the main phase,
172 the geomagnetic activity and interplanetary magnetic field conditions exhibited strong
173 disturbances, whereas monotonic disturbances were observed during the recovery phase.
174 Both IMF B_z and B_y were positive and nearly stable between 1500-2000 UT. The solar wind
175 velocity varied between 600-700 km/s, and solar wind dynamic pressure was approximately
176 2-4 nPa during the period of 1500-2000 UT (shaded area). The solar wind dynamic pressure
177 experienced repeated enhancements around 1600, 1700, and 1820 UT in high solar wind
178 speed environments, in spite of the small magnitudes as shown in Figure 1f-1g (grey shaded
179 areas). The Auroral electrojet indices (AE, AL, AU) did not indicate any substorm activity
180 between 1500-2000 UT, and their maximum values were less than ~ 200 nT (not shown here).

181 **3.2 Geosynchronous particle and magnetic field observations (GOES-16 and GOES-17)**

182 GOES-16 and -17 satellites orbiting in a geostationary orbit have positions of $80^\circ W$ and
183 $\sim 120^\circ W$, respectively, as shown in Figure 1. A notable interval from 1500-2000 UT
184 corresponds to 1027-1508 MLT and 0612-1054 MLT for GOES-16 and -17, respectively.
185 Figure 3 demonstrates (a-d) the magnetic field of the (a) total value (B_t); (b-d) B_e (e is
186 directed radially inward), B_p (p is parallel to the Earth's spin axis), and B_n (n is the
187 azimuthally Earth's spin axis) components as measured by GOES-16 (blue line) and GOES-

188 17 (black line); and (e) GOES-16 electron fluxes plotted for the four energy channels ~131,
189 186, 271, and 380 keV. It is notable that at the 1600 UT boundary, the GOES-16 magnetic
190 field oscillation mode significantly changed from poloidal (including compressional) to the
191 toroidal mode, such that noticeable oscillations of the Bp and Be components were transitioned
192 to amplified Bn oscillations.

193 In addition, the amplified oscillations were observed for the GOES-16 electron flux from
194 1600-1800 UT (Figure 3e), corresponding to near noon time, however not to the dawn sector
195 (GOES-17 located), as tick-labeled in MLT. Significantly smaller amplitude oscillations of
196 Bn were also observed in GOES-17 at the same time (Figure 3d), indicating that GOES-17
197 was farther from the source region of the oscillations than GOES-16.

198 To determine the oscillation frequency of Bn and the electron flux, Figure 3 (g-h and j-k)
199 depicts a periodic analysis using Morlet wavelet analysis (Torrence and Compo., 1998) and
200 the Lomb-Scargle (LS) method (Lomb, 1976). Figures 3f and 3i display the temporal
201 variations in the magnetic Bn and electron flux (at 131 keV), respectively; the middle panels
202 (g and j) display the wavelet spectrogram analysis, and the bottom panels (h and k) display
203 the LS periodogram. For the periodogram analysis of the Pc5 frequency band, the long-term
204 low-frequency region was removed using the third-order Savitzky-Golay smoothing
205 algorithm (Savitzky & Golay 1964). Wavelet analyses of Bn (Figure 3g) and electron flux
206 (Figure 3j) demonstrated spectral power enhancement in a narrow band (5-10 min) of ULF
207 Pc5 waves. This spectral power enhancement lasted for more than 2 hours. The LS analysis
208 reveals dominant discrete periodicities at 7 and 9.8 min (2.4 mHz and 1.8 mHz) in Bn (Figure
209 3h) and at 5.5-6.5 min and 9-9.8 min in the electron flux (Figure 3k).

210 **3.3 Ground-based ionospheric measurements (SuperDARN/Magnetometer/ GPS TEC)**

211 Figure 4 shows measurements of the Saskatoon (SAS) SuperDARN HF radar at a high
212 latitude in the northern hemisphere (Geog/Geom: 52.16° N, 106.63° W/60.88° N, 40.88° W)
213 between 1500-2000 UT. The left panel represents the line of sight (LOS) Doppler velocities
214 with positive (blue) velocity when approaching the radar and negative (red) velocity when
215 away from the radar, and (the right panel) for echo power (dB) derived from beam numbers
216 (bm) of 0 and 12. Clear oscillations appear in both (a-b) LOS velocities and (g-h) echo power
217 from bm 0-12 (not all beams shown here) in the range gates of 12-28 that are corresponding
218 to 675-1395 km slant range and Geog./Geom. latitude of 57-63°N/65-71°N at a time interval

219 1720-1740 UT. Figures 4c and 4i exhibit average values of echo power and LOS velocity
220 from gates 14 to 24 for bm 0 (red) and 12 (green). The magnetic local time (MLT) is taken
221 into consideration at the average locations for range gates 14-24 for bm 0 and 12 (Geog:
222 60°N, -95°W; and 60°N, -85°W, respectively).

223 The wavelet spectrum of the average power and LOS velocity is displayed in Figures 4d-e
224 and 4j-k, in which common dominant periods are found to be 7-10 min (1.67-2.4 mHz) from
225 the enhanced spectral power for LOS velocity and echo power between 1630 and 1800 UT
226 (10:15-11:37 MLT for bm 00, 11:16-12:40 MLT for bm 12). A Lomb-Scargle periodogram
227 analysis was performed for the mean values over the gates of 14-24 of bm 0 and 12, as shown
228 in Figures 4f and 4l. The results of the periodic signature common here are at 7 and 9 min
229 (2.4 mHz and 1.8 mHz) for the LOS rate and at ~9 min for the echo power. The SAS radar's
230 LOS velocity and echo power allowed us to observe discrete frequencies of 1.8 and 2.4 mHz
231 in the Pc5 wave band, identical to the magnetometer Bn component of GOES-16. This may
232 be due to the field of view (bm 12) of the SuperDARN SAS radar, which specifically targets
233 a common area, the GOES-16 footprint.

234 The Pc5 wave oscillations were mostly observed before and after the local noon local in the
235 magnetometer observations. Figure 5 shows the meridional profile of the magnetometer data
236 for the American sector. In Figures 5a and 5d, the northward magnetic field (H-component)
237 variations are presented from high to low latitudes in the northern hemisphere at the time
238 interval of 1500-2000 UT. The locations of the sites are listed in Table 1. Using the Savitzky-
239 Golay smoothing algorithm, the third-order fit line in the H variations was used to eliminate
240 low-frequency components. Figure 5 shows the quasi-monochromatic pulsations. Periodic
241 oscillations were observed three times at approximately 1600, 1700, and 1810 UT (gray
242 shades) from high to low latitudes, corresponding to three times the pressure enhancement as
243 shown in Figure 2g. Smaller oscillations up to lower latitudes were present throughout the
244 entire period and large-amplitude oscillations dominated between 1700 UT and 1740 UT.

245 Figures 5b and 5e show periodogram analysis for H component. Here, two major
246 periodicities appear consistently, mainly at 9.5 and 11.2 min (~1.7 and 1.4 mHz) in the Pc5
247 frequency band along the longitudinal sector (8-12 MLT). In particular, it is noticeable that
248 the periodicity of 9.5 minutes is maintained without shifting from 80°N to 14°N. Here
249 discrete spectrum frequencies (1.4 and 1.7 mHz) can be identified near the FLR frequencies
250 (1.3 and 1.9 mHz) (Samson et al., 1991, 1992; Harrold and Samson, 1992). Wavelet analysis
251 of the H component revealed power spectrum enhancement between 1600 and 1900 UT

252 (Figures 5c and 5f), which was centered in the periodic range between 7-12 min (2.3-1.3
253 mHz). The wavelet power spectra also show that three amplitude enhancements occurred at
254 1600, 1700, and 1810 UT with each lasting approximately ~50 min.

255 Figure 6a shows the vertical TEC variations from high to low latitudes at selected GPS
256 locations across the American longitudinal sector. Figure 6a (leftmost column) shows the
257 GPS TEC variations from high to low latitudes in the following order: YELL (GPS-24:
258 62.4°N, 115.4°W), CHUR (GPS-10: 58.7°N, 94.4°W), KUJ (GPS-23: 55.2°N, 77.1°W),
259 HNPT (GPS-32: 38.5°N, 76.4°W), MDO (GPS-32: 21.4°N, 102.4°W), and BOGT (GPS-23:
260 4.4°N, 74.4°W). The TEC variations and polynomial fits obtained using the third-order
261 Savitzky-Golay algorithm are plotted in black and red, respectively. A periodogram analysis
262 of TEC residual, after the long-term trend was subtracted by the polynomial fit, was
263 performed to examine the small-scale fluctuations. The residual TEC is shown in Figure 6b.
264 Figure 6c shows periodogram analysis results of a common dominant periodicity at 8-9 min
265 (1.8-2.0 mHz) over the high-low latitudes, and for high latitudes (55°- 62°N) longer periods
266 of 11-12 min (1.4-1.5-mHz) also appear. The wavelet power spectrum clearly shows the
267 dominant frequencies in the band of the Pc5 ULF waves between 1600-1800 UT except at the
268 mid-latitude station of the HNPT. The wavelet power spectrum also clearly shows dominant
269 periodicities of 5-15 min (3.3-1.1 mHz) between 1600-1800 UT.

270

271 Figure 7 shows a direct comparison of (a, b) solar wind conditions (V_{sw} , P_{dyn}), (c, f)
272 magnetospheric and (d-e, g-h, i-l) ionospheric Pc5 oscillations: (c-d) oscillations of the
273 azimuthal component (B_n) of the magnetic field at GOES-16 and the northward magnetic
274 field component (H) at FCC; (e) LOS velocity average between gates 14-24 for beams 00
275 (red); and 12 (green); and (f-h) the variations of GOES-16 electron flux, SuperDARN power,
276 and GPS TEC (at YELL); (i and k) ground H component at SJG and KOU; and (j and l) GPS
277 TEC at MDO and BOGT. Here, it is remarkable that three wave packets are noticeable in the
278 B_n and ground H components from high to -low latitudes, as well as in SAS LOS and echo
279 power with a time delay, and TEC with corresponding to three repeating P_{dyn} enhancements
280 at ~1600, ~1700, and ~1800 UT (indicated with grey shades). The ULF wave activity and
281 amplitude enhancement of ionospheric and magnetospheric oscillations appear to be
282 significantly linked to pressure pulse enhancements. In the modulated ionospheric and
283 magnetospheric parameters, a strong common periodicity is found as 7.6 and 9.7 min (2.1 and
284 1.7 mHz).

285 **4. Discussion**

286 This section discusses the observations presented in the previous section and attempts to
287 make case for an observational link between wave activity in the magnetosphere and
288 ionosphere. The common periodicities of 7.5 and 9.7 min (2.2 and 1.7 mHz) in the eastward
289 component of the GOES-16 magnetic field (Bn), electron flux intensities, magnetometer data,
290 SupeDARN, and GPS TEC were observed during the magnetic storm's recovery phase on
291 November 4, 2021. These oscillations evident ns were most noticeable in the geomagnetic
292 field and ionospheric density and, which occurred simultaneously from high to low latitudes.

293 **4.1 Pc5 pulsations at high latitude in H- component, GPS TEC, and SuperDARN radar**

294 Several studies have been conducted on Pc5 pulsations and have shown distinctive
295 characteristics for each type of oscillation (Ruohoniemi et al., 1991; Walker et al., 1992;
296 Harrold and Samson, 1992; Lester et al., 2000; Ponomarenko et al., 2001; Sakaguchi et al.,
297 2012; Norouzi-Sedeh et al., 2015; Belakhovsky et al., 2016; Fenrich et al., 2019; Kozyreva et
298 al., 2020). Pc5 pulsations can be generated by the Kelvin-Helmholz instability at
299 magnetospheric boundaries as of standing Alfvén waves in a tube with FLRs. FLRs are
300 magnetospheric magnetic perturbations in the azimuthal direction of toroidal mode waves.
301 The FLR signatures in the magnetometer data can be seen in the magnetic north-south or H
302 component owing to the rotational effect of the ionosphere or Hall currents. However,
303 poloidal mode waves are characterized by magnetic field perturbations in the radial direction,
304 which induce perturbations in the magnetic east-west or D component (Hughes, 1983; Chen
305 and Hasegawa, 1991).

306 In our observations, oscillations in the magnetic H-component in the magnetometer data
307 could be linked to toroidal mode waves (Bn) or FLRs induced by the solar wind dynamic
308 pressure because magnetic field perturbations between 1600-1900 UT in the magnetosphere
309 are only seen in the azimuthal component (Bn), not in Be or Bp (Figure 3). Additionally,
310 toroidal mode waves are responsible for the simultaneously observed common periods of 7.5
311 and 9.5 min (2.2 and 1.7 mHz) in the Bn and H components, respectively. Previous studies
312 have reported that Pc5 pulsations with discrete frequencies of 1.3, 1.9, 2.6, 3.4, and 4.2 mHz
313 have been observed from high-latitude ground-based magnetometers triggered by FLRs or
314 driven by magnetospheric waveguide modes (Samson et al., 1991, 1992; Harrold and Samson,
315 1992; Ruohoniemi et al., 1991). Wright and Rickard (1995) suggested that magnetospheric

316 waveguide modes can be excited by solar wind turbulence at the magnetopause to produce
317 pulsation. According to their studies, running pulses generated by the solar wind, which are
318 predicted to be features of Kelvin-Helmholtz surface waves, can produce magnetopause
319 ripples, waveguide modes, and FLRs with phase velocities equal to the speed of the running
320 pulse. The three-wave packets of Pc5 pulsations observed in GOES-16 Bn and the electron
321 flux, H (high-low latitude), SuperDARN LOS velocity and echo power, and TEC
322 observations, can be the result of FLR due to repeated pressure intensification.

323 In poloidal modes, the wave electric field oscillates azimuthally while the wave magnetic
324 field oscillates radially; conversely, in toroidal mode, the wave electric field is radially
325 polarized while the wave magnetic field and velocity perturbations are azimuthally polarized
326 (Hudson et al., 2004). Toroidal waves are more efficiently coupled to compressional
327 disturbances at larger azimuthal scales than poloidal waves (Radoski, 1967). The toroidal Pc5
328 pulsations can be excited by the KHI at the magnetopause stimulated by high solar wind
329 speed and/or the dynamic pressure enhancements, followed by the propagation of a fast
330 magnetosonic wave deep into the magnetosphere and the generation of FLRs. Some of this
331 energy is transformed into standing Alfvén waves along field lines when a fast magnetosonic
332 wave travels deep into the magnetosphere; the SuperDARN and ground-based
333 magnetometers can detect these standing Alfvénic waves (Fenrich et al., 1995; Sung et al.,
334 2006; Harrold and Samson, 1992; Lester et al., 2000; Ponomarenko et al., 2001). When
335 pulsations occur on the magnetic field lines elongated from the magnetosphere to the
336 ionosphere, the associated pulsating E field causes the local bulk ionosphere to move with an
337 $E \times B$ drift, which can be monitored by SuperDARN HF radar. The field-aligned irregularities
338 at ionospheric heights also experience this force and travel at varying velocities. This
339 movement manifested as a periodic variation in the LOS velocity as recorded by SuperDARN.
340 The ionospheric velocity oscillations observed by the SAS radar as shown in Figure 4a-c are
341 linked to toroidal mode waves, as the compressional disturbance can modulate the Alfvén
342 wave magnetic field and velocity perturbations in the azimuthal directions. As a result, the
343 high latitude ionospheric convection electric field and $E \times B$ flow drift can be modulated. The
344 changes of the electric field may be magnified by fast magnetosonic standing Alfvén waves
345 moving along the field lines, so that the azimuthal component (Bn) and LOS velocity were
346 observed to have common periods of 7.5 and 9.5 min (2.2 and 1.7 mHz). The oscillation
347 pattern with three wave packets was also clearly visible in the LOS velocity and Bn
348 corresponding to the repeated pressure enhancement at 1600, 1700, and 1820 UT. In addition,

349 the convection maps in the northern hemisphere (not shown here) were repeatedly enlarged
350 and contracted along with the LOS velocity oscillations and echo power. Positive line-of-
351 sight velocity was observed toward the radar as the dusk (dawn) convection cell expanded
352 (contracted), and negative ionospheric velocity was observed as the dusk (dawn) cell
353 contracted (expanded) during that time. As demonstrated in the SuperDARN beam 0 data
354 oscillations, the period of negative LOS velocity (away from the radar) for 7.5 min or 9.7 min
355 corresponded to the echo power increase. As the SAS radar beam 0 looks toward the
356 magnetic north pole, negative velocity increase signified the increase in the poleward
357 (antisunward) convection velocity near noon. As a result, we can surmise that the ionospheric
358 density increases during the enhanced convection electric field. Pc5 pulsation can
359 periodically drive the convection electric field, resulting in the transfer of the magnetospheric
360 electron flux into the ionosphere by precipitation along the magnetic field line.

361 According to Watson et al. (2015), the ULF modulation of energetic electron precipitation
362 may lead to additional periodic ionization of the lower ionosphere, resulting in periodic TEC
363 variations that are much more significant than variations in the geomagnetic field. The theory
364 of Alfvén wave interaction with the thin ionospheric layer can also be used to interpret the
365 simultaneous periodic variations in ionospheric plasma velocity and geomagnetic field.
366 Belakhovsky (2016) examined the TEC modulation by magnetospheric Alfvén waves and
367 proposed that several possible mechanisms, including periodic plasma heating, convection
368 across a steep gradient, and field-aligned electron transport, could work simultaneously. In
369 some cases, magnetospheric precipitating energetic electron fluxes that are modulated by Pc5
370 pulsations can also efficiently modulate the ionospheric density (Sarris et al., 2007; Pilipenko
371 et al., 2014a, 2014b). In our observations, ionospheric density observed with the proxy of
372 SuperDARN radar echo power and GPS TEC exhibited periodic oscillations similar to those
373 of energetic electron flux at common periodicities of 7.5 and 9.7 min (2.2 and 1.5 mHz) as
374 shown in Figure 4g-l, 6, and 3i-k, respectively. The interaction of electromagnetic
375 hydrodynamic (MHD) waves with the ionosphere can cause ionospheric density modulation.
376 This is evident from the observation of B_n, electron flux, LOS, and H-component oscillating
377 with the same period. Correspondingly, the same mechanism can be expected to cause the
378 TEC modulations via Pc5 waves.

379 **4.2 Pc5 pulsations at low latitude in H component and GPS TEC**

380 The ULF pulsations in the ionosphere are typically a combination of Alfvén and

381 compressional fast magnetosonic (FMS) waves. Numerous ground, satellite, and radar
382 observations at high latitudes have demonstrated that Pc5 waves in the ionosphere are
383 primarily composed of Alfvén waves (Wright and Rickard., 1995; Samson et al. 1991; Sung
384 et al., 2006; Harrold & Samson, 1992; Lester et al., 2000; Mathie & Mann., 2000; Pilipenko
385 et al. 2014a, 2014b). Pilipenko et al. (2014a) reported that ULF modulation effects can be
386 observed not only at auroral latitudes but also at low latitudes. The transmission of Pc5 waves
387 to lower and equatorial latitudes is most likely explained by a non-Alfvénic mechanism, such
388 as the cavity or MHD waveguide modes. Previous studies suggested the fast magnetosonic
389 waveguide mode for TEC modulations in ULF Pc5 waves at the middle and low latitudes
390 (Marin et al., 2014; Belakhovsky., 2016; Vorontsova et al, 2016).

391 Vorontsova et al. (2016) presented a combined study of TEC and magnetometer observations
392 at the low latitude and provided crucial details regarding the physical mechanism of Pc5
393 pulsations. They suggested that the TEC modulations at low latitudes were caused by plasma
394 compression via the fast magnetosonic mode. As the FMS waveguide mode arrives in the
395 low-latitude ionosphere, it provokes periodic modulation of the TEC and the magnetic field
396 response on the ground. From our observations, periodic oscillations of the TEC and
397 magnetic field H component at low latitudes can be explained by a scenario that the FMS
398 waveguide mode enters the low latitude ionosphere, causing periodic oscillations with
399 periods of 7.5 and 9.7 minutes (2.2 and 1.7 mHz) as shown in Figure 5. The FMS waveguide
400 mode could be induced by impulses in dynamic pressure during high solar wind speed
401 (Figure 7). Pc5 pulsations have been observed at equatorial and low latitudes, and several
402 studies have investigated and provided different explanations for their occurrence (Ziesolleck
403 and Chamalaun 1993; Reddy et al. 1994; Shinohara et al., 1998; Motoba et al. 2002; Huang
404 2021). Ziesolleck and Chamalaun (1993) examined the spatial characteristics of the Pc5
405 pulsations associated with large-scale cavity resonances, global compressional modes, and
406 direct incoming hydromagnetic waves at lower latitudes. In contrast to the effects of directly
407 incoming hydromagnetic waves at lower latitudes, electric field penetration from high
408 latitudes to the equator can be responsible for electric field oscillations in the ExB at lower
409 latitudes (Reddy et al. 1994; Shinohara et al., 1998; Motoba et al. 2002). As the geomagnetic
410 and interplanetary conditions were quiet and of small magnitude during our observations, we
411 assumed that the possibility of penetration of the electric field was relatively low. The
412 presented results lend more credence to sudden impulses in the dynamic pressure and solar
413 wind velocity dependent mechanism.

414 **5. Conclusion**

415 We investigated the monochromatic Pc5 pulsations observed in magnetosphere and
416 ionosphere in the noon (10-14 MLT, 1600-1900 UT) on November 4, 2021, during the
417 recovery phase of the magnetic storm. The events were synchronized with repeated dynamic
418 pressure enhancements during high solar wind speeds, but without significant interplanetary
419 magnetic field activity remained in positive B_y and positive B_z . Observations from GOES-16,
420 the ground magnetometers, SuperDARN, and GPS-TEC measurements consistently revealed
421 common ULF Pc5 discrete frequency oscillations in the magnetosphere and high-to-low
422 latitude ionosphere.

423 The main findings of this study are:

- 424 1. In the magnetosphere and high-to-low latitude ionospheres, periods of 7.5 and 9.7 min
425 (2.2 and 1.7 mHz) were simultaneously observed in GOES-16 azimuthal component of
426 magnetic field (B_n) and electron flux for the magnetosphere, H component, SuperDARN
427 LOS velocity and echo power, and GPS TEC for the high-to-low ionospheres, in the noon
428 sector of 10-14 MLT.
- 429 2. A series of three monochromatic oscillation packets occurred commonly in B_n , high-to-
430 low latitude ground H-component (north-south), SuperDARN LOS velocity and echo
431 power, and GPS-TEC (high-low latitudes) by three times small enhancements of solar
432 wind dynamic pressure during high solar wind speeds.
- 433 3. From SuperDARN (bm 0) data oscillations, the period of negative LOS velocity (away
434 from the radar) for 7.5 min and 9.7 min corresponded to echo power increase. This
435 signifies that the ionospheric density increases during the enhancement of poleward
436 convection velocity caused by the enhanced convection electric field.
- 437 4. Notably, the dominant Pc5 discrete frequency of 1.7 mHz observed in the magnetosphere
438 (B_n) and high latitudes (H) remained persistent to low latitudes without change.
- 439 5. The amplified modulation of the GOES-16 B_n component signifies the magnetic field
440 oscillation active in toroidal field line resonance in the magnetosphere, which can affect
441 the oscillations of the H component, SuperDARN LOS velocity and echo power, and
442 GPS TEC at high latitudes based on observations of their oscillations at the same discrete
443 frequency.

444 6. Pc5 oscillations in radar power (dB) and TEC at high latitudes can be caused by
445 magnetospheric Alfvén waves, field-aligned transport, and periodic magnetospheric
446 electron precipitation.

447 7. The oscillations in the TEC and H components are attributed to the fast magnetosonic
448 (FMS) waveguide mode.

449 In summary, multiple observations reveal common oscillations of ULF Pc5 discrete
450 frequencies at 2.2 and 1.7 mHz in the magnetosphere and high-to-low latitude ionosphere.
451 Enhancement of solar wind dynamic pressure during high solar wind speeds can induce
452 toroidal mode FLR modulation in the magnetosphere. The modulation of the ionospheric
453 density, convection velocity, and TEC in the Pc5 frequency at high latitudes can be attributed
454 to the FLR effect, and the Pc5 modulations of H-component and TEC in the low latitudes
455 ionosphere are likely caused by the cavity mode and fast magnetosonic (FMS) waveguide.

456 **Acknowledgments**

457 This work was supported by the National Research Foundation of Korea (NRF) grant funded
458 by the Korea Government (MSIP) (NRF-2021R1A2C1005306). We acknowledge the ERG
459 (Exploration of Energization and Radiation in Geospace) project team for the provision of the
460 ground-based observation (SuperDARN) data. We also thank the scientific team (PI, Dr.
461 Kathryn McWilliams) for the data provision from the Saskatoon SuperDARN radar. We
462 thank GSFC/SPDF OMNIWeb for the solar wind parameters and geomagnetic activity
463 indices. We thank all the GOES project PIs for the magnetospheric data. We also thank the
464 SuperMAG magnetometer network and CARISMA teams for the magnetometer data.

465 **Data Availability Statement**

466 OMNI data are available at https://spdf.gsfc.nasa.gov/pub/data/omni/high_res_omni/.
467 SuperDARN cdf formatted data are available [https://ergsc.isee.nagoya-](https://ergsc.isee.nagoya-u.ac.jp/data/ergsc/ground/radar/sd/fitacf/)
468 [u.ac.jp/data/ergsc/ground/radar/sd/fitacf/](https://ergsc.isee.nagoya-u.ac.jp/data/ergsc/ground/radar/sd/fitacf/). GOES satellites and GPS TEC data can be found at
469 <https://www.ngdc.noaa.gov/stp/satellite/> and <https://cddis.nasa.gov/pub/gps/data>. The
470 magnetometer data are available from the SuperMAG magnetometer network
471 (<http://supermag.jhuapl.edu>) and the Canadian Array for Real-time Investigations of
472 Magnetic Activity (CARISMA) (<https://www.carisma.ca/carisma>).

473

474 **References**

475 Allan, W., S. P. White, and E. M. Poulter (1986), Impulse-excited hydromagnetic cavity and
476 field line resonances in the magnetosphere, *Planet. Space Sci.*, 34, 371.

477 Baddeley, L. J., Yeoman, T. K., McWilliams, K. A., & Wright, D. M. (2007). Global Pc5
478 wave activity observed using SuperDARN radars and ground magnetometers during an
479 extended period of northward IMF. *Planetary and Space Science*, **55**, 792– 808.

480 Belakhovsky, V., Pilipenko, V., Engebretson, M., Sakharov, Y., & Selivanov, V. (2019).
481 Impulsive disturbances of the geomagnetic field as a cause of induced currents of electric
482 power lines. *Journal of Space Weather and Space Climate*, 9, A18.

483 Belakhovsky, V., Pilipenko, V., Murr, D. et al. (2016). Modulation of the ionosphere by Pc5
484 waves observed simultaneously by GPS/TEC and EISCAT. *Earth Planet Sp* 68, 102.

485 Boteler, D. H., Pirjola, R. J., & Nevanlinna, H. (1998). The effects of geomagnetic
486 disturbances on electrical systems at the Earth's surface. *Adv. Space Res.*, 22(1), 17–27.

487 Chen, L., & Hasegawa, A. (1974). A theory of long-period magnetic pulsations: 1. Steady-
488 state excitation of field line resonance. *J. Geophys. Res.*, 79(7), 1024–1032.

489 Davies, K., Hartman, G.K. (1976). Short-period fluctuations in total columnar electron
490 content. *J. Geophys. Res.* 81, 3431–3434.

491 Elkington, S. R., M. K. Hudson, and A. A. Chan (1999). Acceleration of relativistic electrons
492 via drift-resonant interaction with toroidal-mode Pc5 ULF oscillations, *Geophys. Res. Lett.*,
493 26, 3273.

494 Fenrich, F. R., Gillies, D. M., Donovan, E., & Knudsen, D. (2019). Flow velocity and field
495 aligned current associated with field line resonance: SuperDARN measurements. *Journal of*
496 *Geophysical Research: Space Physics*, 124, 4889–4904.

497 Fenrich, F. R., J. C. Samson, G. Sofko, and R. A. Greenwald (1995). ULF high- and low-m
498 field line resonances observed with the Super Dual Auroral Radar Network, *J. Geophys. Res.*,
499 100, 21,535–21,548, doi:10.1029/95JA02024.

500 Hamada, A.M., Mahrous, A.M., Fathy, I., Ghamry, E., Groves, K., Yumoto, K. (2015). TEC
501 variations during geomagnetic storm/substorm with Pc5/Pi2 pulsation signature. *Adv. Space*
502 *Res.* 55, 2534–2542.

503 Harrold, B. G., and J. C. Samson (1992), Standing ULF modes of the magnetosphere: A
504 theory, *Geophys. Res. Lett.*, 19, 1811. Hughes, W. J. (1974). The effect of the atmosphere
505 and ionosphere on long period magnetospheric micropulsations. *Planetary and Space*
506 *Science*, 22(8), 1157– 1172.

507 Harrold, B. G., and J. C. Samson (1992). Standing ULF modes of the magnetosphere: A

508 theory, *Geophys. Res. Lett.*, 19, 1811.

509 Huang, C.-S. (2021). Global Pc5 pulsations from the polar cap to the equator: Wave
510 characteristics, phase variations, disturbance current system, and signal transmission. *J.*
511 *Geophys. Res.*, 126, e2020JA029093.

512 Hudson, M. K., R. E. Denton, M. R. Lessard, E. G. Miftakhova, and R. R. Anderson (2004).
513 A study of Pc-5 ULF oscillations, *Ann. Geophys.*, 22, 289.

514 Jacobs, J. A., Kato, Y., Matsushita, S., & Troitskaya, V. A. (1964). Classification of
515 geomagnetic micropulsations. *J. Geophys. Res.*, 69(1), 180–181.

516 Kivelson, M., Pu, Z. (1984). The Kelvin-Helmholtz instability on the magnetopause.
517 *Planetary and Space Science* 32, 1335–1341.

518 Kivelson, M.G., Southwood, D.J. (1986). Coupling of global magnetospheric MHD
519 eigenmodes to field line resonances. *Journal of Geophysical Research* 91, 4345–4351.

520 Kozyreva, O. V., Pilipenko, V. A., Bland, E. C., Baddeley, L. J., & Zakharov, V.
521 I. (2020). Periodic modulation of the upper ionosphere by ULF waves as observed
522 simultaneously by SuperDARN radars and GPS/TEC technique. *Journal of Geophysical*
523 *Research: Space Physics*, 125, e2020JA028032.

524 Lester, M., Davies, J. A., & Yeoman, T. K. (2000). The ionospheric response during an
525 interval of Pc5 ULF wave activity. *Annales Geophysicae*, 18, 257–261

526 Lomb, N. R. (1976). Least-squares frequency analysis of unequally spaced data, *Astrophys.*
527 *Space Sci.*, 39, 447–462.

528 Mann, I. R., A. N. Wright, K. J. Mills, and V. M. Nakariakov (1999). Excitation of
529 magnetospheric waveguide modes by magnetosheath flows, *J. Geophys. Res.*, 104, 333.

530 Marin J, Pilipenko V, Kozyreva O, Stepanova M, Engebretson M, Vega P, Zesta E. (2014).
531 Global Pc5 pulsations during strong magnetic storms: excitation mechanisms and
532 equatorward expansion. *Ann Geophys* 32:319–331.

533 Mathie, R. A., and I. R. Mann (2000). Observations of Pc5 field line resonance azimuthal
534 phase speeds: A diagnostic of their excitation mechanism, *J. Geophys. Res.*, 105, 10,713.

535 Motoba, T., Kikuchi, T., Lühr, H. et al., (2002). Global Pc5 caused by a DP 2-type
536 ionospheric current system. *J. Geophys. Res.*, 107(A2).

537 Norouzi-Sedeh, L., Waters, C. L., & Menk, F. W. (2015). Survey of ULF wave signatures
538 seen in the Tasman International Geospace Environment Radars data. *Journal of Geophysical*
539 *Research: Space Physics*, 120, 949–963.

540 Pilipenko V, Belakhovsky V, Kozlovsky A, Fedorov E, Kauristie, K. (2014b). ULF wave

541 modulation of the ionospheric parameters: radar and magnetometer observations. *J Atmos*
542 *Sol-Terr Phys* 108:68–76.

543 Pilipenko, V., Belakhovsky, V., Murr, D., Fedorov, E., Engebretson, M. (2014a). Modulation
544 of total electron content by ULF Pc5 waves. *J. Geophys. Res.* 119, 4358–4369.

545 Ponomarenko, P. V., Waters, C. L., Sciffer, M. D., & Fraser, B. J. (2001). Spatial structure of
546 ULF waves: Comparison of magnetometer and Super Dual Auroral Radar Network data.
547 *Journal of Geophysical Research*, 106, 10,509–10,517.

548 Radoski, H. R. (1967). A note on oscillating field lines, *J. Geophys. Res.*, 72(1).

549 Reddy, C. A., Ravindran, S., Viswanathan, K. S. et al. (1994). Observations of Pc5
550 micropulsation-related electric field oscillations in the equatorial ionosphere. *Ann. Geophys*,
551 12, 565–573.

552 Ruohoniemi, J. M., R. A. Greenwald, K. B. Baker, and J. C. Samson (1991). HF radar
553 observations of Pc 5 field line resonances in the midnight/early morning MLT sector,
554 *Geophys. Res. Lett.*, 96, 15,697.

555 Sakaguchi, K., Nagatsuma, T., Ogawa, T., Obara, T., & Troshichev, O. A. (2012).
556 Ionospheric Pc5 plasma oscillations observed by the King Salmon HF radar and their
557 comparison with geomagnetic pulsations on the ground and in geostationary orbit. *Journal of*
558 *Geophysical Research*, 117, A03218.

559 Samson, J. C. et al., (1991) Magnetometer and radar observations of MHD cavity modes in
560 the Earth's magnetosphere, *Can. J. Phys.*, **69**, 929–937.

561 Samson, J. C., B. G. Harrold, J. M. Ruohoniemi, and A. D. M. Walker (1992). Field line
562 resonances associated with MHD waveguides in the magnetosphere, *Geophys. Res. Lett.*, 19,
563 441-444.

564 Sarris, T.E., Loto'aniu, T.M., Li, X., and Singer, H.J. (2007). Observations at
565 geosynchronous orbit of a persistent Pc5 geomagnetic pulsation and energetic electron flux
566 modulations, *Ann. Geophysicae*, 2007, vol. 25, pp. 1653-1667.

567 Savitzky, A., & Golay, M. J. E. (1964). Smoothing and differentiation of data by simplified
568 least squares procedures. *Analytical Chemistry*, 36, 1627–1639.

569 Shinohara, M., Yumoto, K., Hosen, N., Yoshikawa, A., Tachihara, H., Saka, O. et al. (1998).
570 Wave characteristics of geomagnetic pulsations across the dip equator. *J. Geophys. Res.*,
571 103(A6), 11745–11754.

572 Skone, C., Nicholson, N. (2006). Detection and mitigation of geomagnetic pulsation effects
573 using GPS. In: ION GNSS 2006, Session D3, Fort Worth, Texas.

574 Southwood, D. J. (1974). Some features of field line resonances in the magnetosphere, *Planet.*
575 *Space Sci.*, 22, 483.

576 Southwood, D. J., and M. G. Kivelson (1990). The magnetohydrodynamic response of the
577 magnetospheric cavity to changes in solar wind pressure, *J. Geophys. Res.*, 95(A3), 2301 –
578 2309.

579 Sung, SK., Kim, KH., Lee, DH. et al., (2006). Simultaneous ground-based and satellite
580 observations of Pc5 geomagnetic pulsations: A case study using multipoint
581 measurements. *Earth Planet Sp* 58, 873–883.

582 Torrence, C., & Compo, G. P. (1998). A practical guide to wavelet analysis. *Bulletin of the*
583 *American Meteorological Society*, 79, 61–78.

584 Vorontsova E, Pilipenko V, Fedorov E, Sinha A. K, Vichare, G. (2016). Modulation of total
585 electron content by global Pc5 waves at low latitudes. *Adv Space Res* 57:309–319.

586 Walker, A.D.M., Ruohoniemi, J.M., Baker, K.B., Greenwald, R.A., Samson, J.C. (1992),
587 Spatial and temporal behavior of ULF pulsations observed by the Goose Bay HF radar.
588 *Journal of Geophysical Research*, 12187–12202.

589 Watson C, Jayachandran PT, Singer HJ, Redmon RJ, Danskin D. (2015). Large amplitude
590 GPS TEC variations associated with Pc5–6 magnetic field variations observed on the ground
591 and at geosynchronous orbit. *J Geophys Res.* doi:10.1002/2015JA021517.

592 Wright, A. N., and G. J. Rickard (1995). ULF pulsations driven by magnetopause motions:
593 Azimuthal phase characteristics, *J. Geophys. Res.*, 101, 24,991.

594 Yagova, N. V., Pilipenko, V. A., Sakharov, Y. A., & Selivanov, V. N. (2021). Spatial scale of
595 geomagnetic Pc5/Pi3 pulsations as a factor of their efficiency in the generation of
596 geomagnetically induced currents. *Earth Planets and Space*, 73(1), 88.

597 Ziesolleck, C. W. S., & Chamalaun, F. H. (1993). A two-dimensional array study of low-
598 latitude PC 5 geomagnetic pulsations. *J. Geophys. Res.*, 98 (A8), 13703–13713.

599 Ziesolleck, C. W. S., Fenrich, F. R., Samson, J. C., & McDiarmid, D. R. (1998). Pc5 field
600 line resonance frequencies and structure observed by SuperDARN and CANOPUS. *Journal*
601 *of Geophysical Research*, 103(A6), 11,771–11,785.

602

603

604

605 **Figure**

606 **Figure 1.** Site map for GPS TEC, ground magnetometers, SuperDARN SAS, and magnetic

607 footprints of the GOES-16 and GOES-17 satellites.

608 **Figure 2.** Solar wind and geomagnetic conditions for 04th November 2021. (a) Solar wind
609 speed (V_{sw} , km/s), (b) solar wind dynamic pressure (P_{dyn} , nPa), (c) IMF B_y (black) and B_z
610 (red) in nT, (d) IEFy (mV/m), and (e) SYM-H (nT). (f-g) Enlarged views of high solar wind
611 speeds (V_{sw}) and three times enhancements of P_{dyn} , matched with the gray-shaded region
612 from 1600-1900 UT.

613 **Figure 3.** (a-e) Magnetic field and electron flux observations from the GOES-16 (blue) and
614 GOES-17 (black) geosynchronous satellite and the Pc5 pulsation analysis for GOES-16: (a)
615 B_t (total magnetic field), (b) B_e (earthward or radial), (c) B_p (azimuthally eastward), (d) B_n
616 (parallel to the earth spin axis), and (e) electron flux intensities in the energy channels ~131,
617 186, 271, 380 keV. For GOES-16 (f, i) B_n and electron flux, (g, j) wavelet power spectrum
618 and (h, j) Lomb-Scargle periodogram, respectively. The grey-shaded regions indicate three
619 times the P_{dyn} enhancements and PC5 pulsations observed.

620 **Figures 4.** (a-b) SuperDARN SAS site line-of-sight (LOS) velocity for beams 00 and 12, (c)
621 average LOS velocity over gates 14 to 24 (red and green line for beams 00 and 12), (d-e)
622 wavelet power spectrum of the LOS average, and (f) the periodogram. The right panels from
623 g-l are the equivalent panels (a-f) except for the echo power.

624 **Figure 5.** (a) Pc5 analysis for ground magnetometers located in the American longitudinal
625 sector: (left) residual after applying Savitzky and Golay algorithm, (middle) periodogram,
626 and (right) wavelet spectrogram for (a-c) high latitudes and (d-f) low latitudes.

627 **Figures 6.** Pc5 analysis for TEC obtained from the GPS sites (numbers) of YELL (GPS-24),
628 CHUR (GPS-10), KIJ (GPS-32), HNPT (GPS-32), MDO (GPS-32), and BOGT (GPS-23)
629 located in the American longitudinal sector: the (a) VTEC (black) and the fitted (red) with
630 Savitzky and Golay algorithm, (b) residual of TEC (c) periodogram, and (d) wavelet
631 spectrogram.

632 **Figures 7** Comparison among solar wind condition and magnetospheric and ionospheric
633 parameters: (a) solar wind velocity (V_{sw}), (b) solar wind dynamics pressure (P_{dyn}), (c)
634 GOES-16 magnetic field (B_n), (d) H-component at FCC, (e) average LOS velocity (bm 00
635 (red) and 12 (green)), (f) GOES-16 electron flux at 131 keV, (g) average power for beams 0
636 (red) and 12 (green), and (h) TEC at YELL including high-latitude sites; for low latitude (i, k)
637 H component and (j, l) TEC oscillations. Pressure pulse enhancements are indicated with
638 gray-shaded regions (a-b).

639

640
 641
 642
 643
 644
 645
 646
 647
 648
 649
 650
 651

Table 1 List of magnetometer and GPS TEC stations used in the analysis and their geographical and geomagnetical coordinates.

Station name	Station CODE	Geographic (Latitude)	Geographic (Longitude)	Geomagnetic (Latitude)	Geomagnetic (Longitude)
Magnetometers					
Resolute	RES	74.5° N	94.8° W	82.3° N	47.2° W
Taloyoak	TALO	69.5° N	93.5° W	77.7° N	35.1° W
Rankin Inlet	RANK	62.8° N	92.1° W	71.2° N	28.3° W
Fort Churchill	FCC	58.7° N	94.0° W	67.0° N	29.2° W
Gillam	GILL	56.3° N	94.6° W	64.5° N	29.0° W
Island Lake	ISLL	53.8° N	94.6° W	62.1° N	28.2° W
Pinawa	PINA	50.1° N	96.0° W	58.3° N	29.1° W
Brandon	BRD	49.8° N	99.9° W	57.6° N	33.7° W
Ottawa	OTT	45.4° N	75.5° W	54.5° N	3.5° W
Sable Island	SBL	43.9° N	60.1° W	51.9° N	15.1° W
Boulder	BOU	40.4° N	105.2° W	47.5° N	37.4° W
Fredericksburg	FRD	38.2° N	77.3° W	47.1° N	5.0° W
Fresno	FRN	37.1° N	119.7° W	42.9° N	52.2° W
Tucson	TUC	32.1° N	87.6° W	39.0° N	16.0° W
Stennis Space Center	BSL	30.3° N	110.7° W	38.8° N	41.5° W
San Juan	SJG	18.1° N	66.1° W	27.1° N	7.1° W
Kourou	KOU	5.2° N	52.7° W	13.9° N	21.2° W
GPS TEC Receivers					
Yellowknife	YELL	62.4° N	114.4° W	68.1° N	56.5° W
CHURCHILL	CHUR	58.7° N	94.4° W	66.3° N	28.8° W
Kuujuarapik	KUJ	55.2° N	77.4° W	64.1° N	5.7° W
Cambridge	HNPT	38.5° N	76.4° W	47.1° N	3.8° W
Fort Davis	MDO	21.4° N	102.4° W	28.23° N	31.5° W
Bogota	BOGT	4.4° N	74.4° W	13.7° N	1.3° W

652

653
654
655
656
657
658
659
660
661
662
663
664
665
666
667
668
669
670
671
672
673
674
675
676

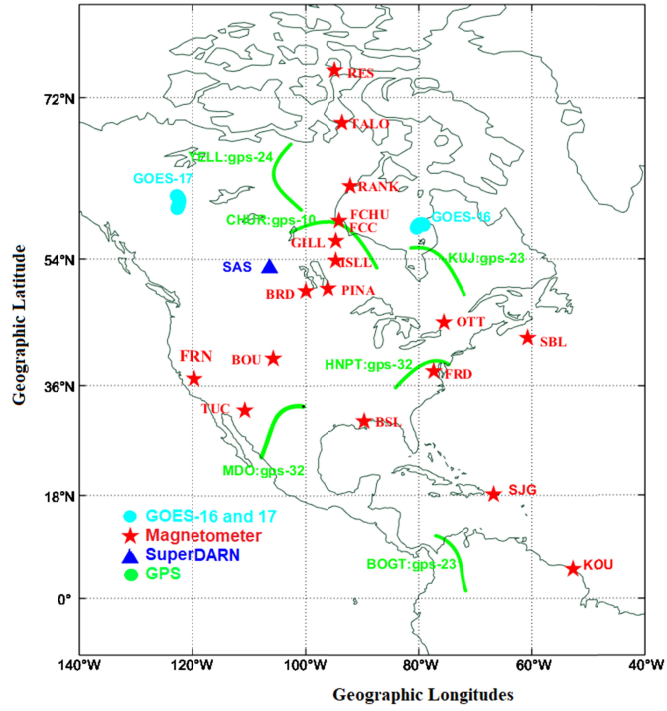


Figure 1

677

678

679

680

681

682

683

684

685

686

687

688

689

690

691

692

693

694

695

696

697

698

699

700

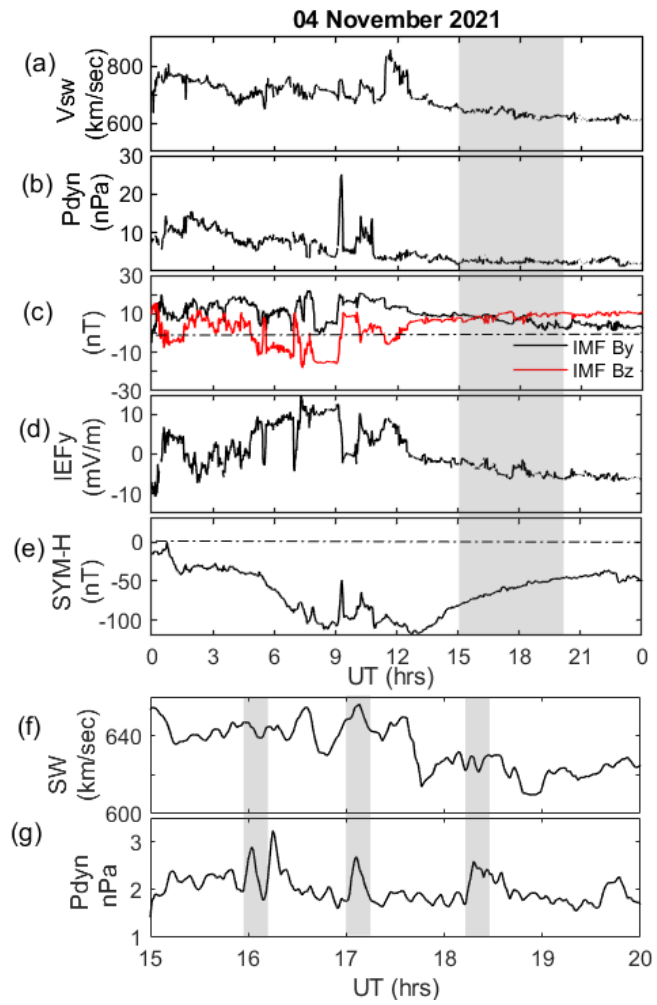
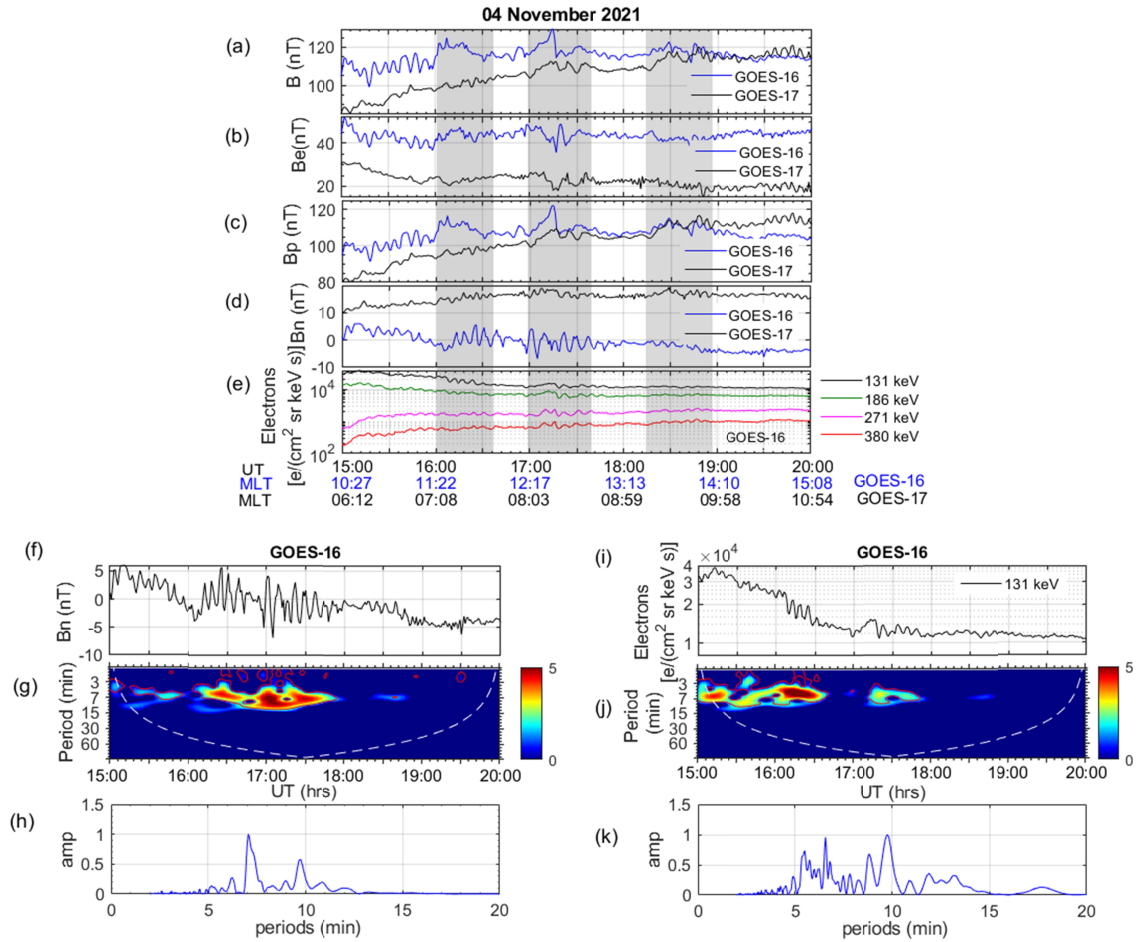


Figure 2

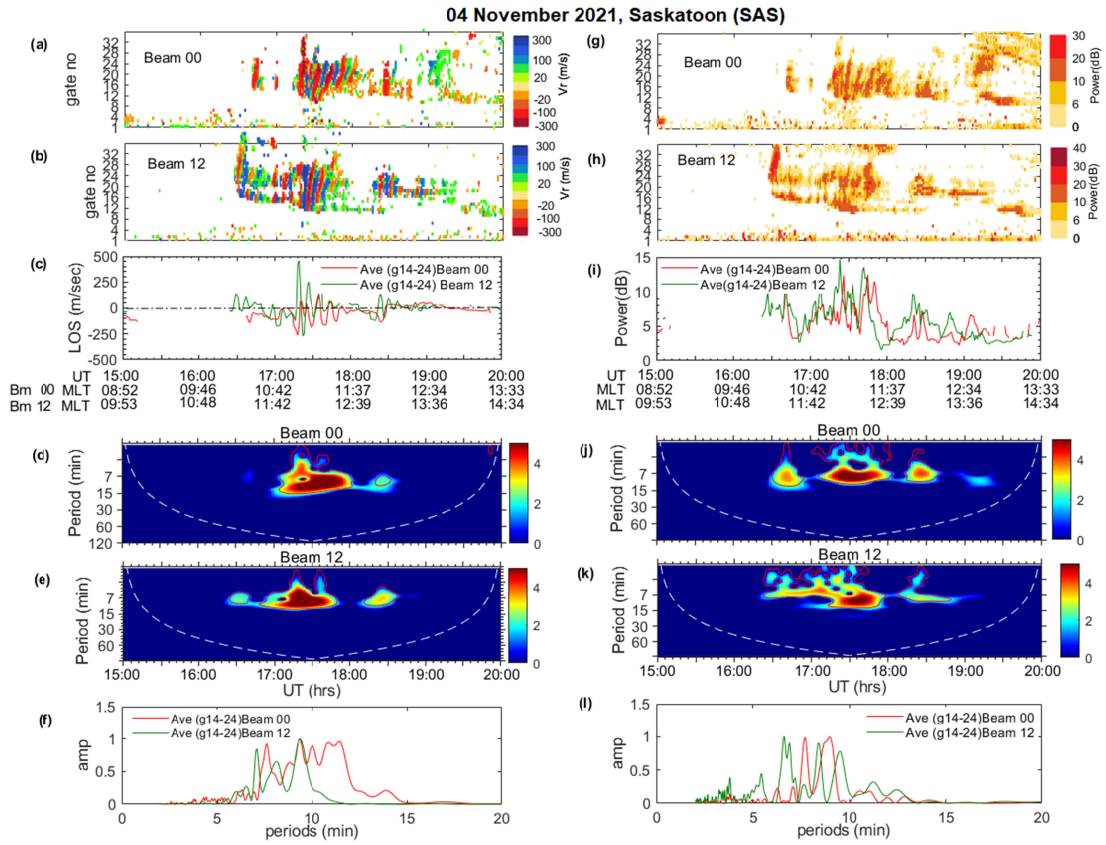
701
702
703



704
705
706
707
708
709
710

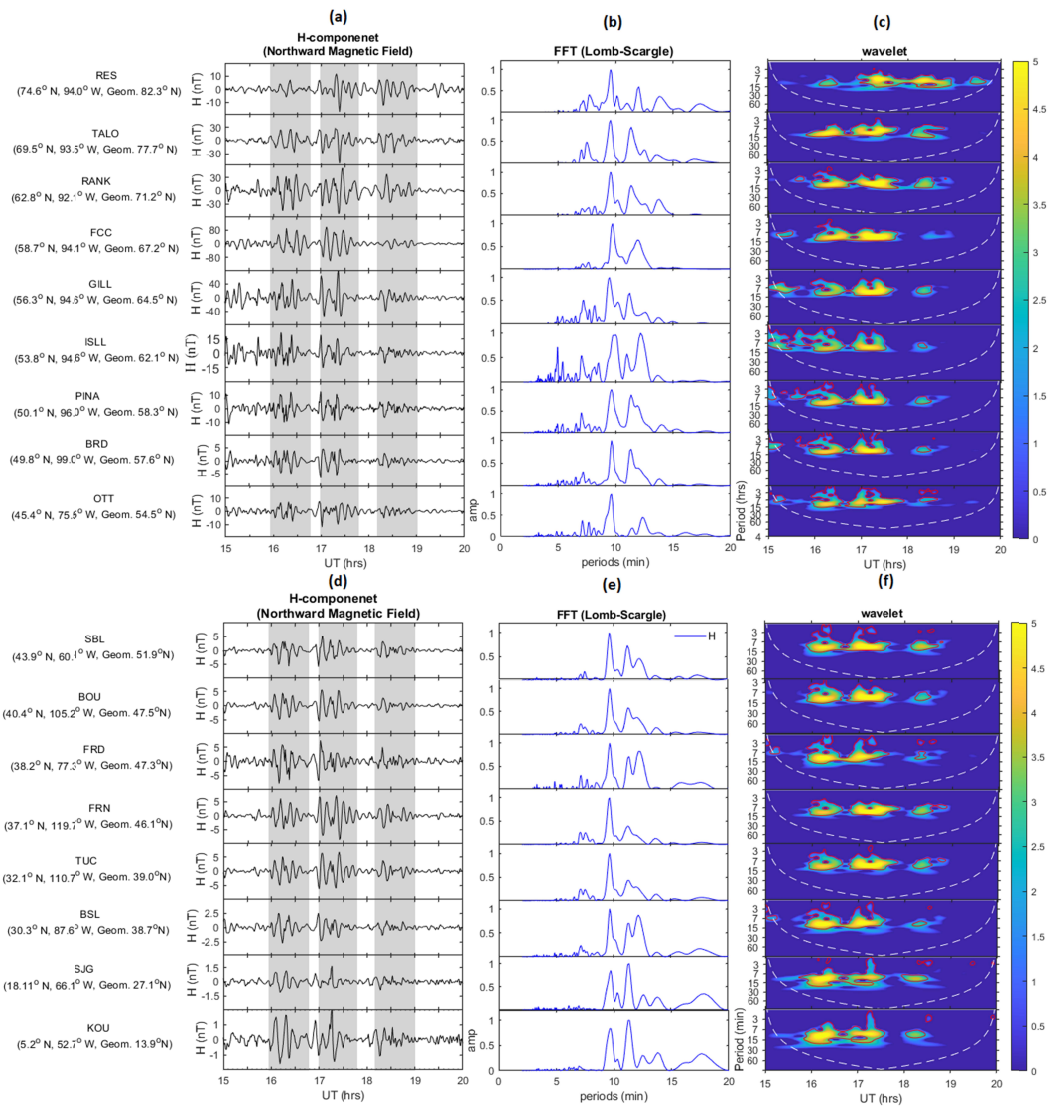
Figure 3

711



712
713
714
715
716
717
718

Figure 4



719

720

721

722

723

724

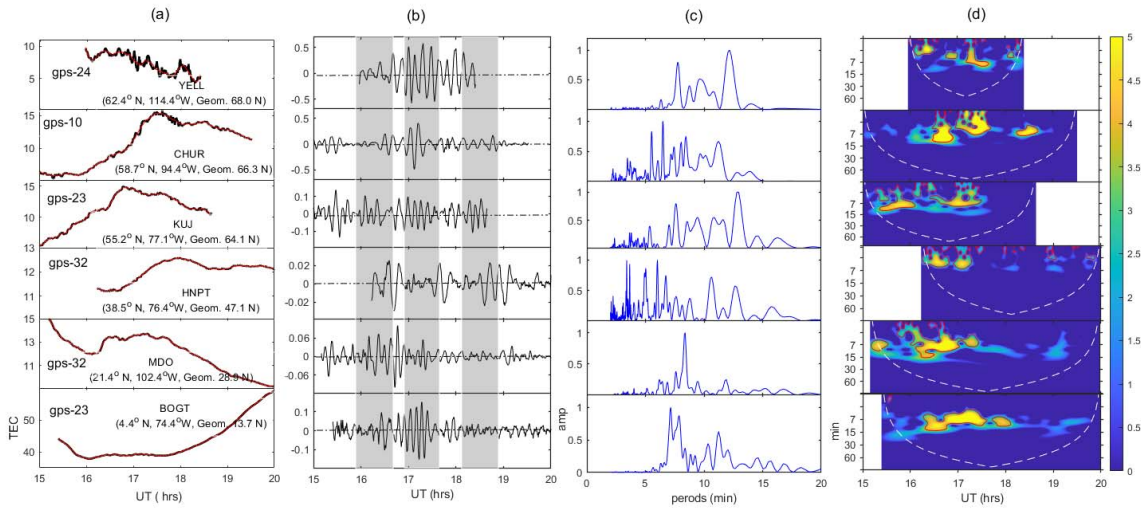
725

726

Figure 5

727

728



729

730

731

732

733

Figure 6

734

735

736

737

738

739

740

741

742

743

744

745

746

747

748

749

750

751

752

753

754

755

756

757

758

759

760

761

762

763

764

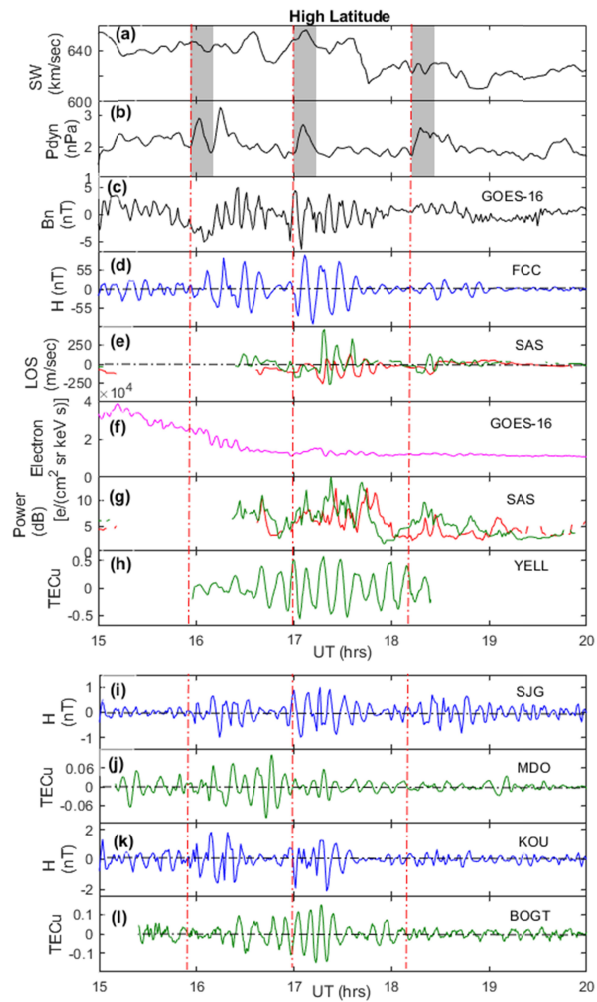


Figure 7

Figure 1.

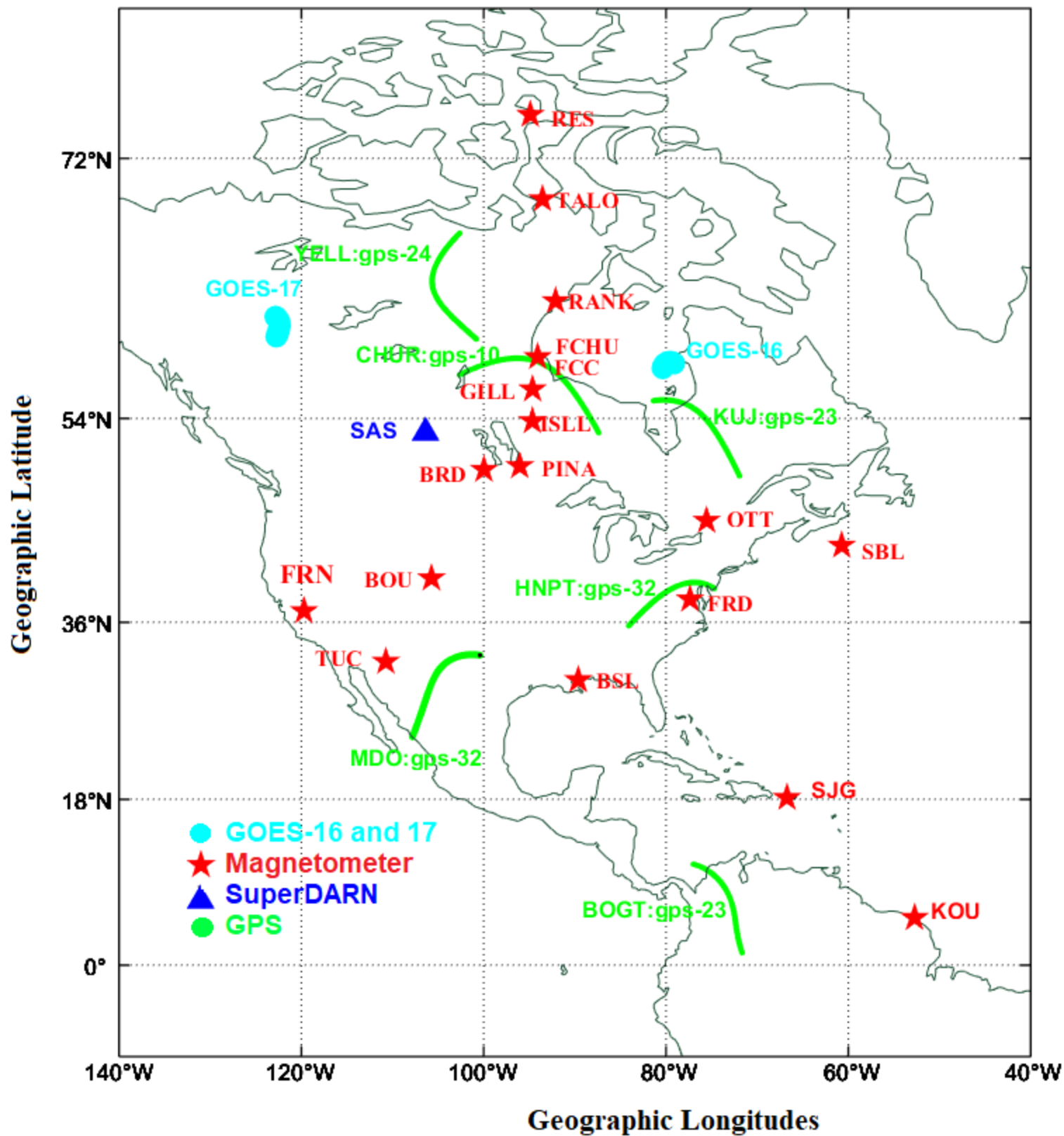


Figure 2.

04 November 2021

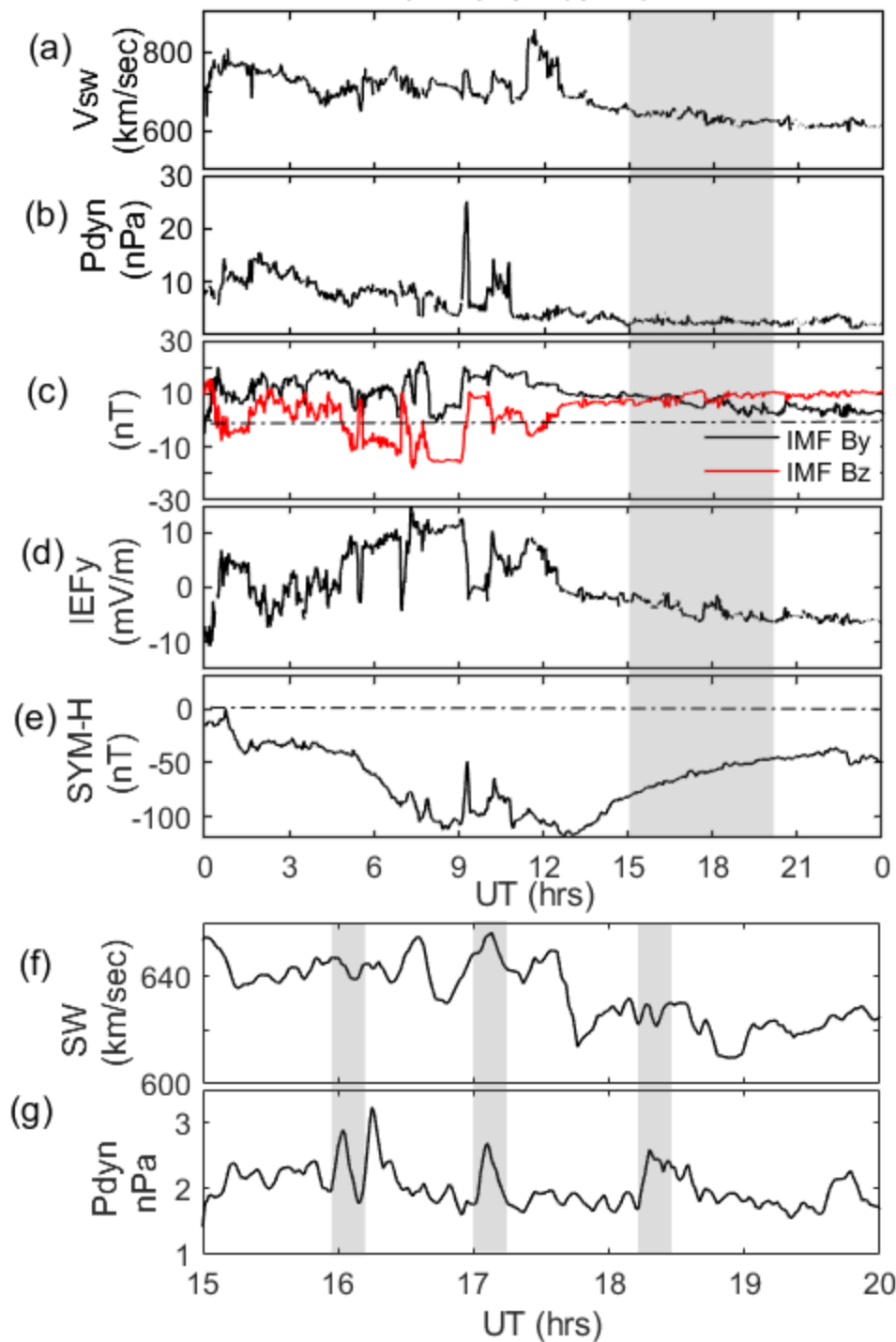


Figure 3.

04 November 2021

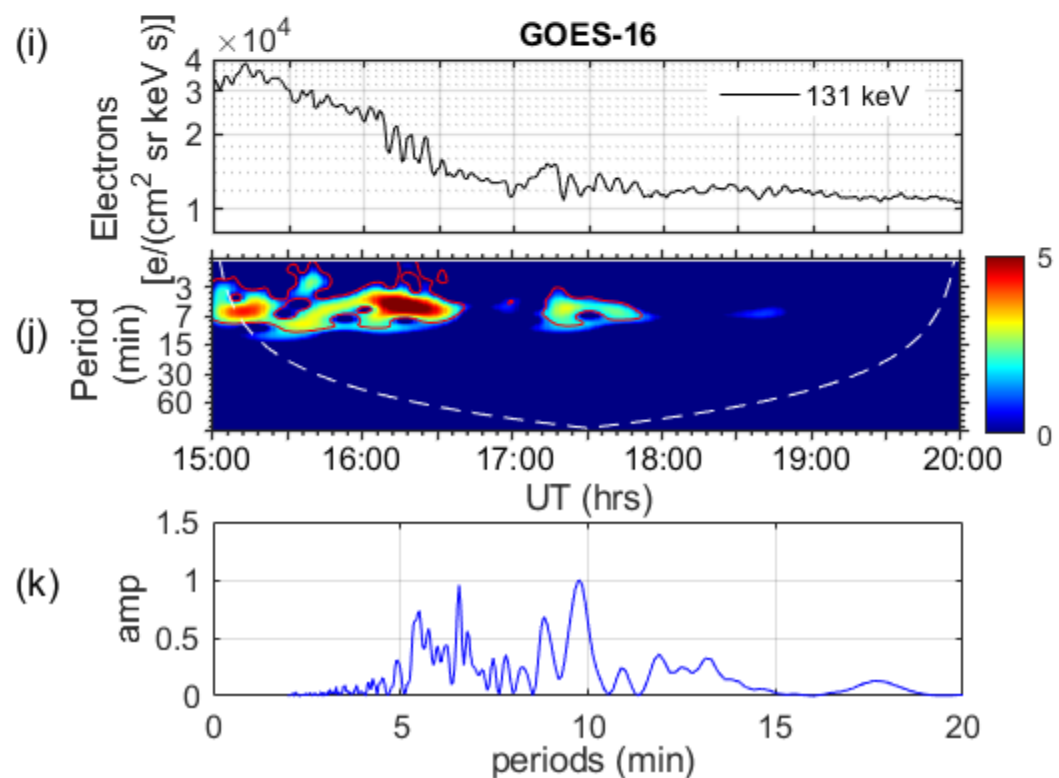
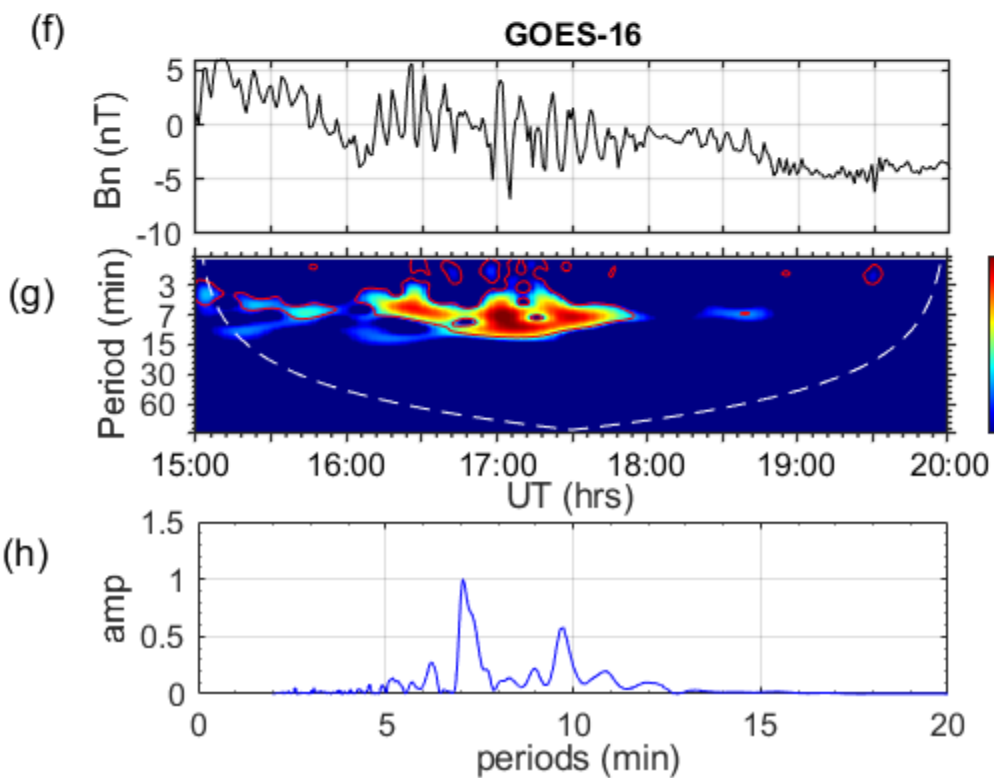
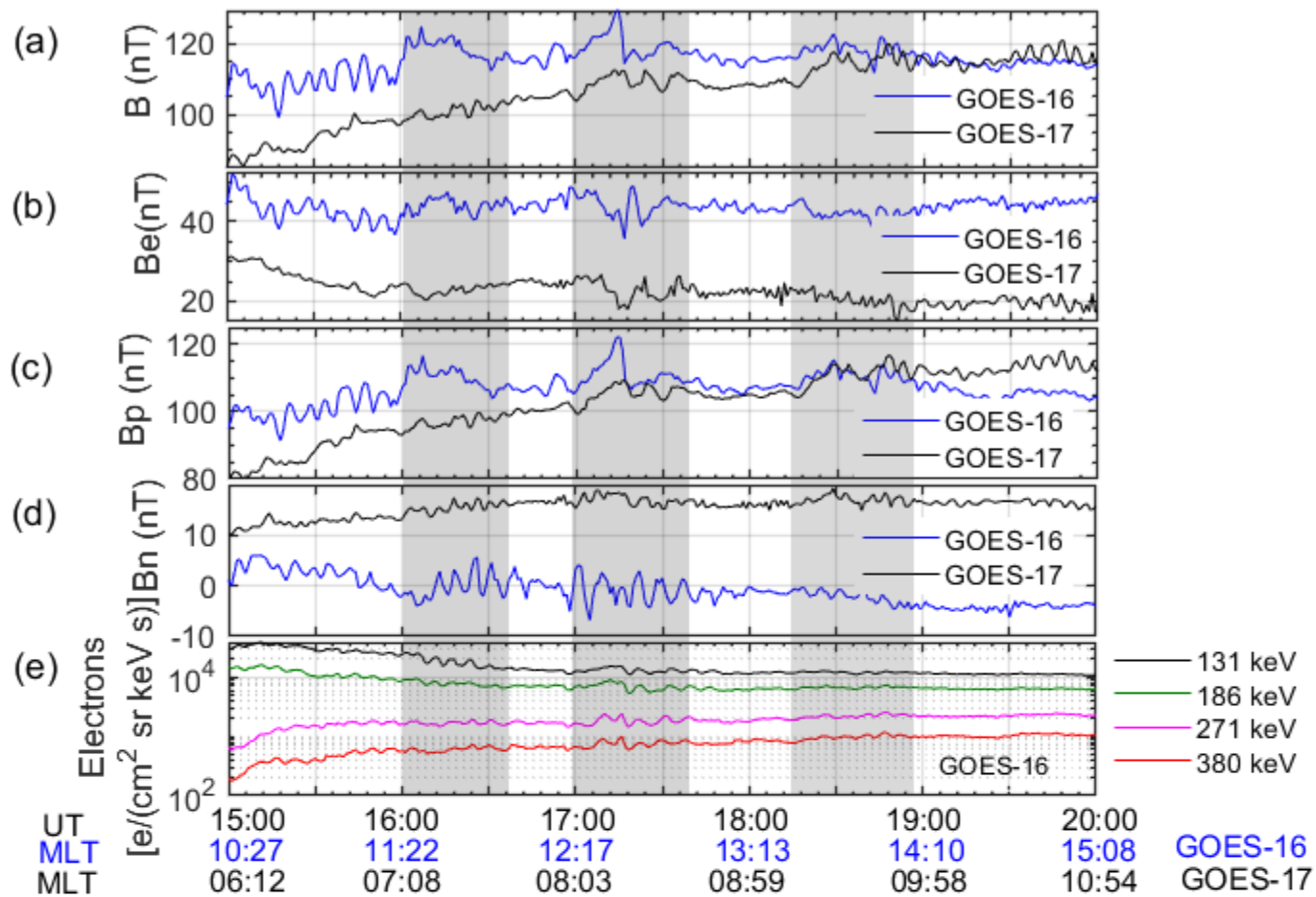


Figure 4.

04 November 2021, Saskatoon (SAS)

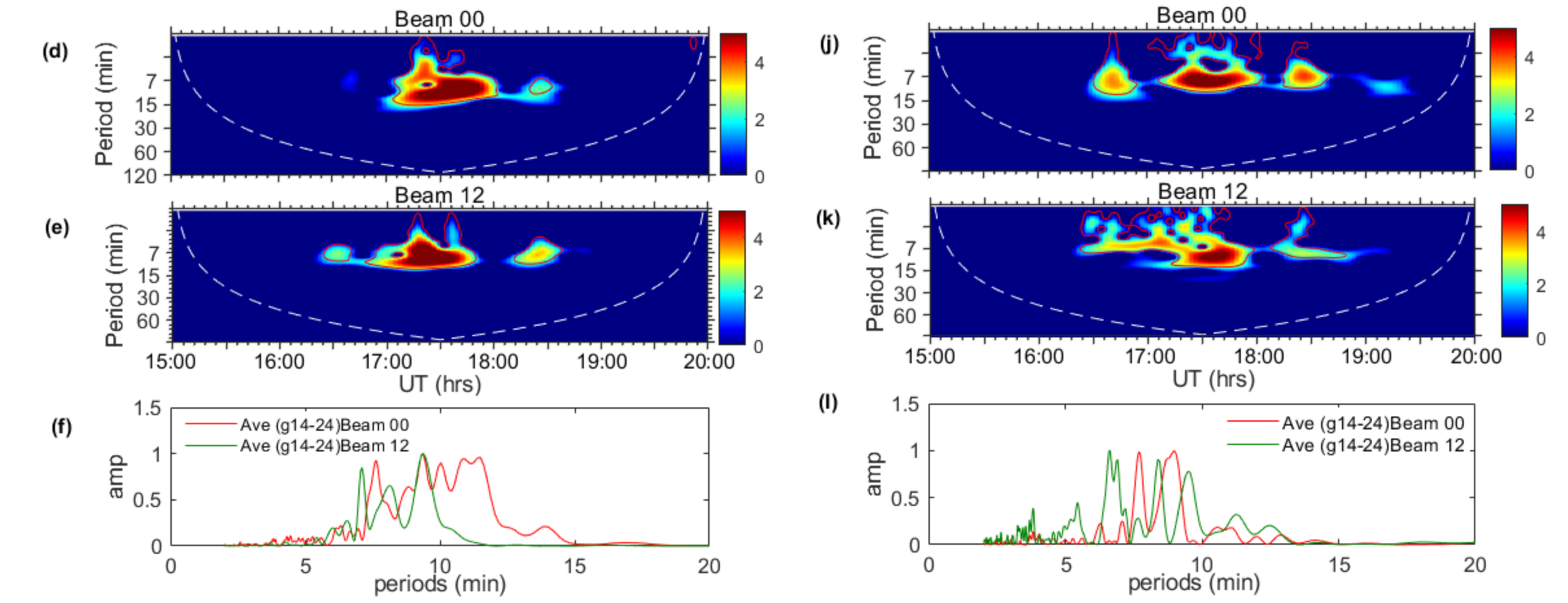
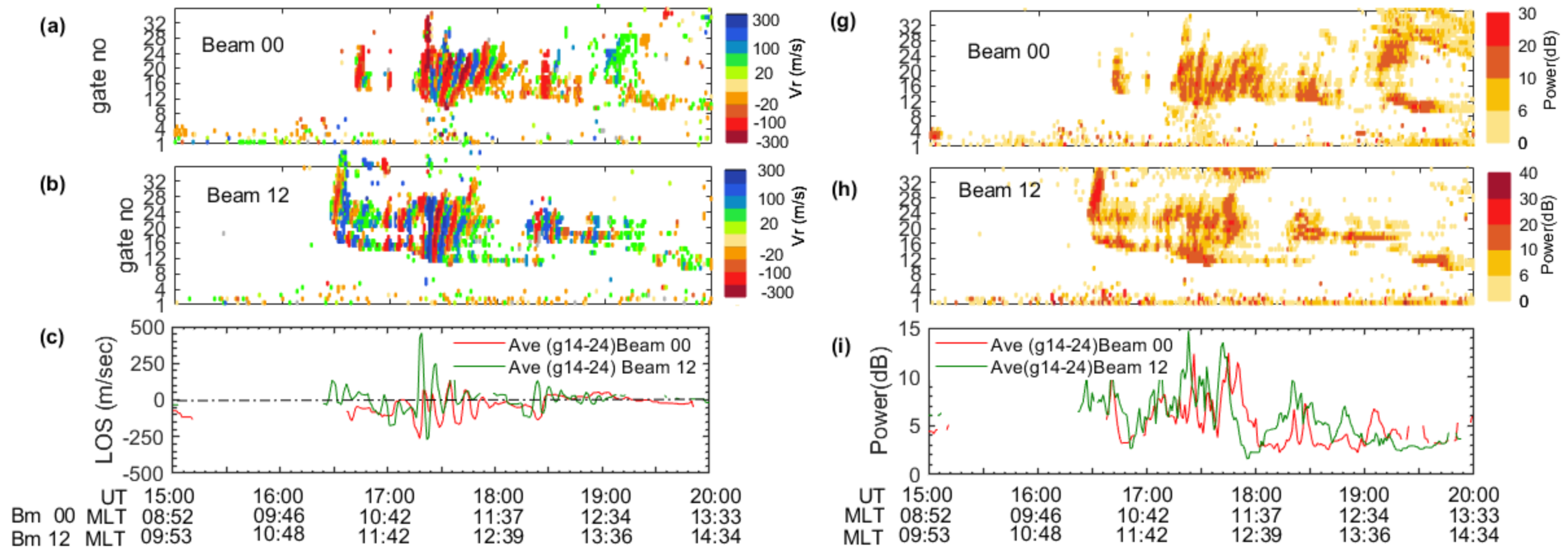


Figure 5.

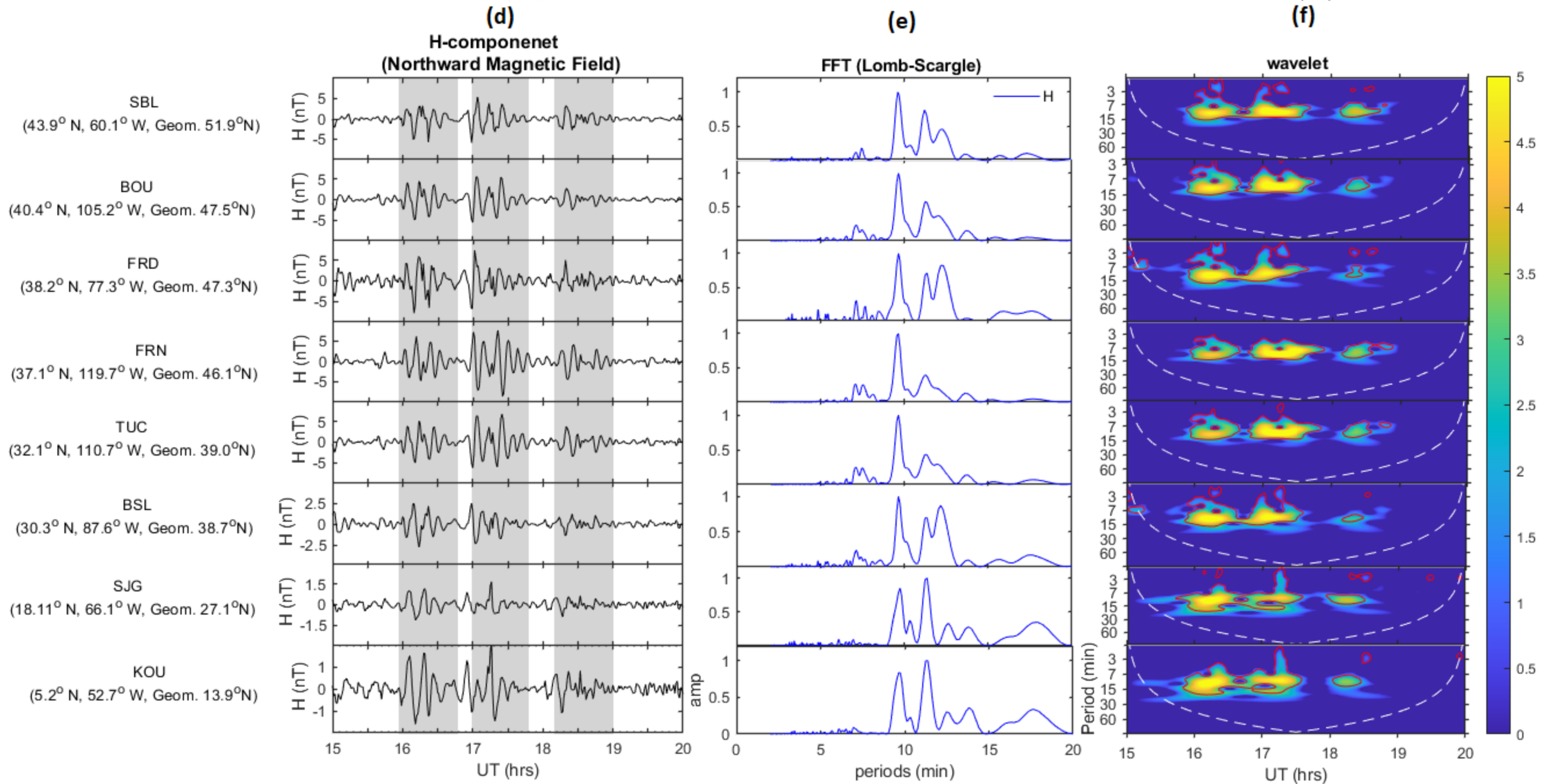
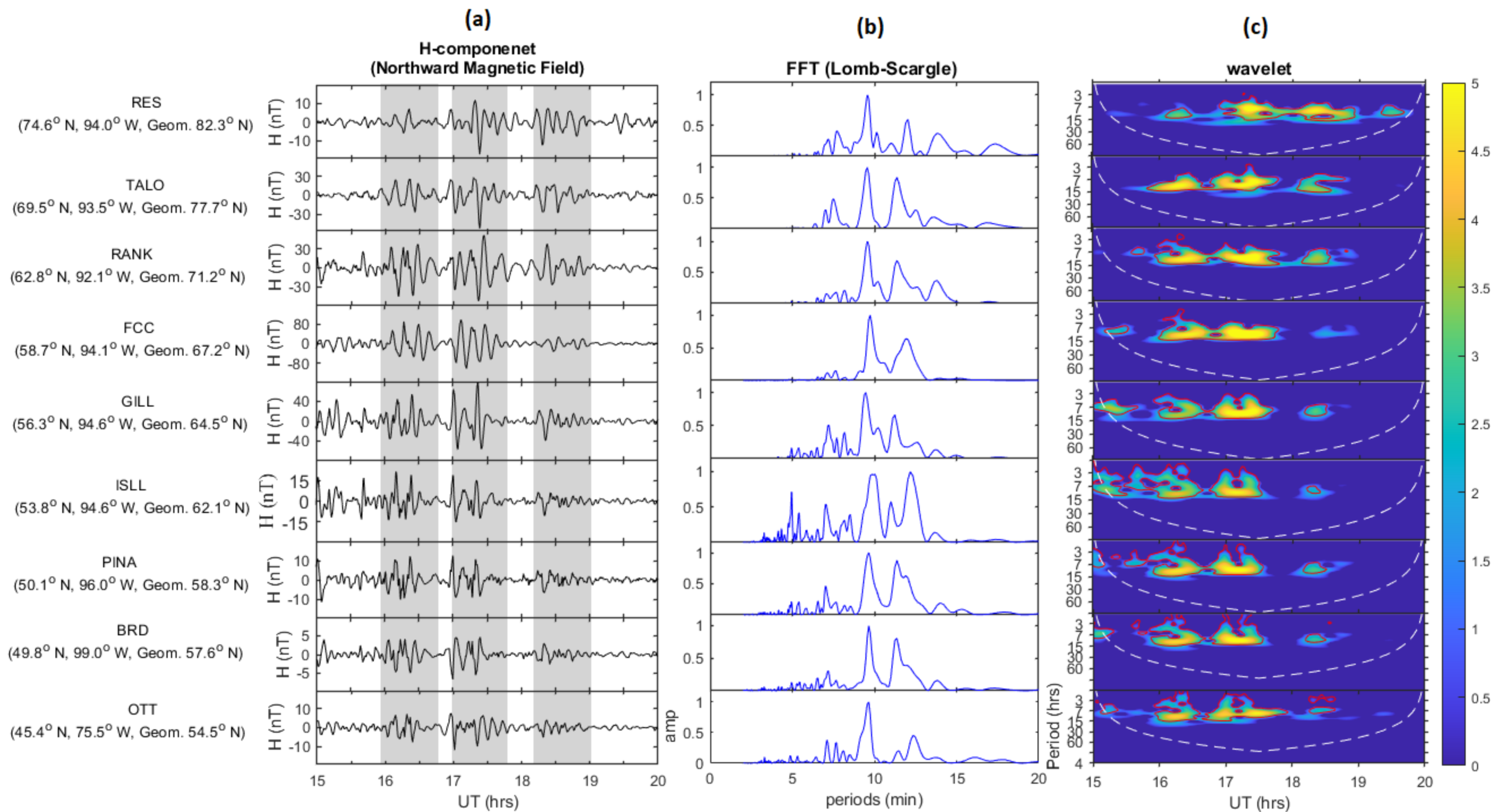
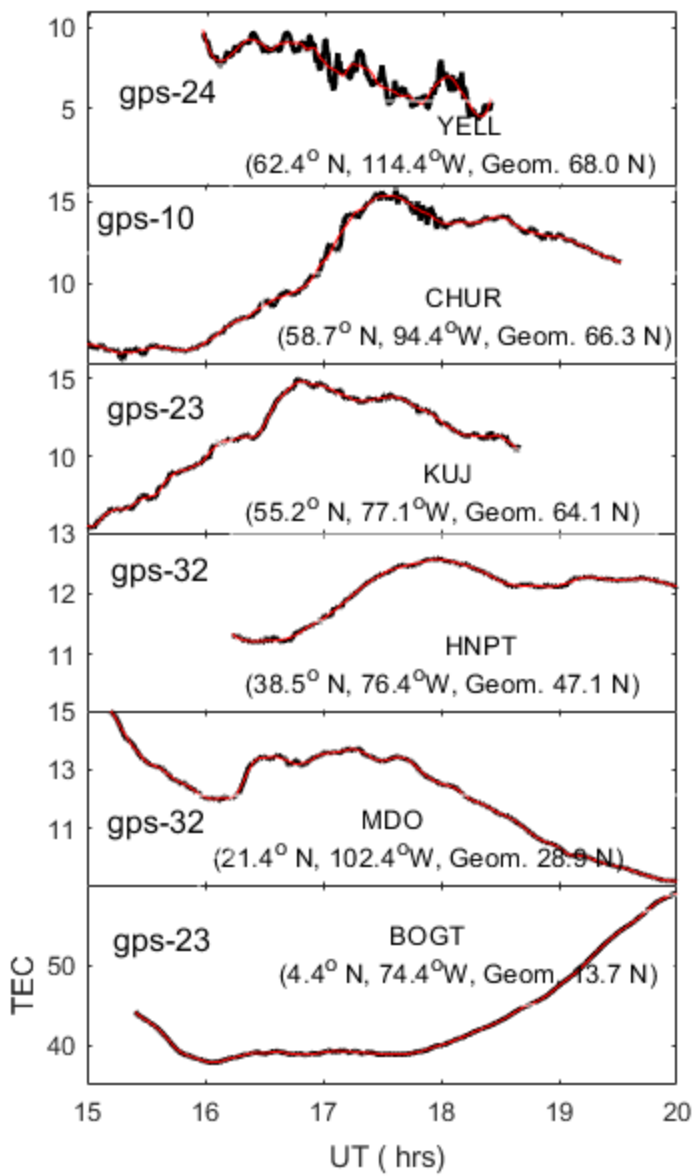
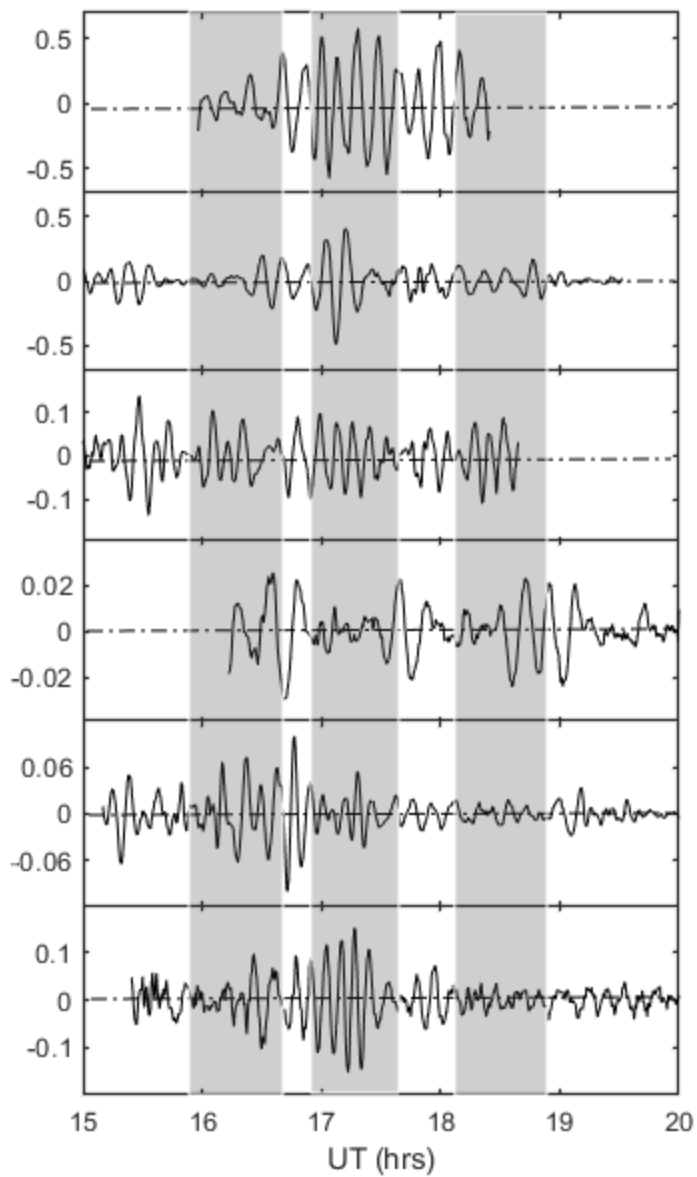


Figure 6.

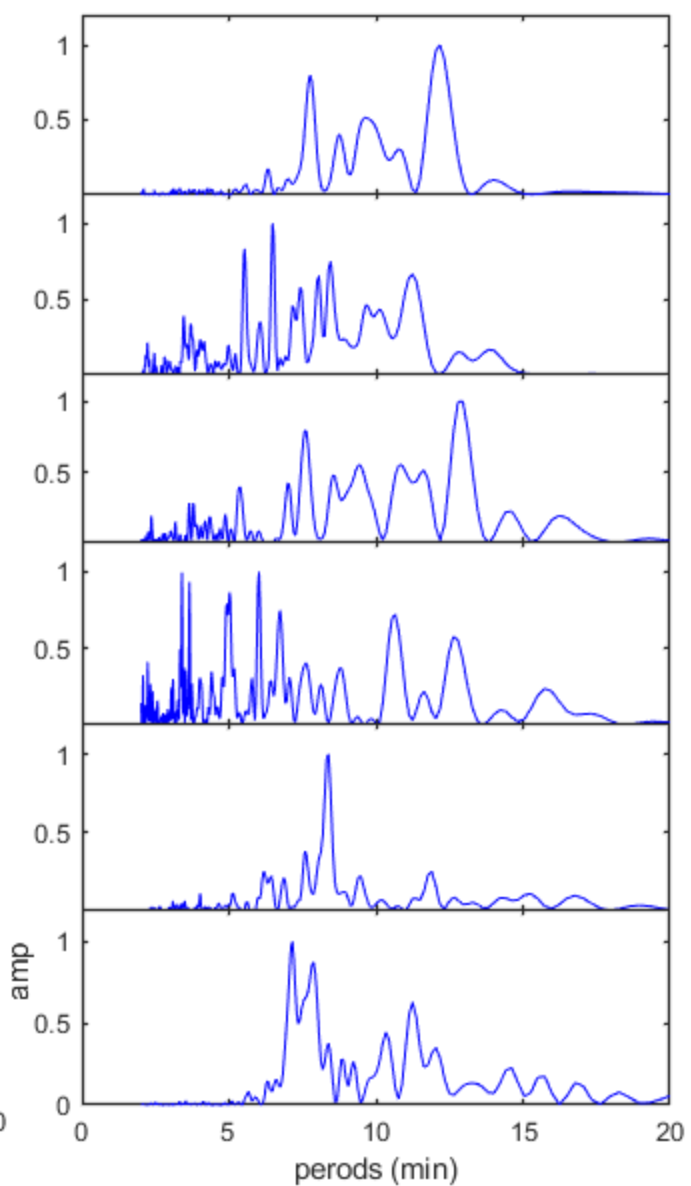
(a)



(b)



(c)



(d)

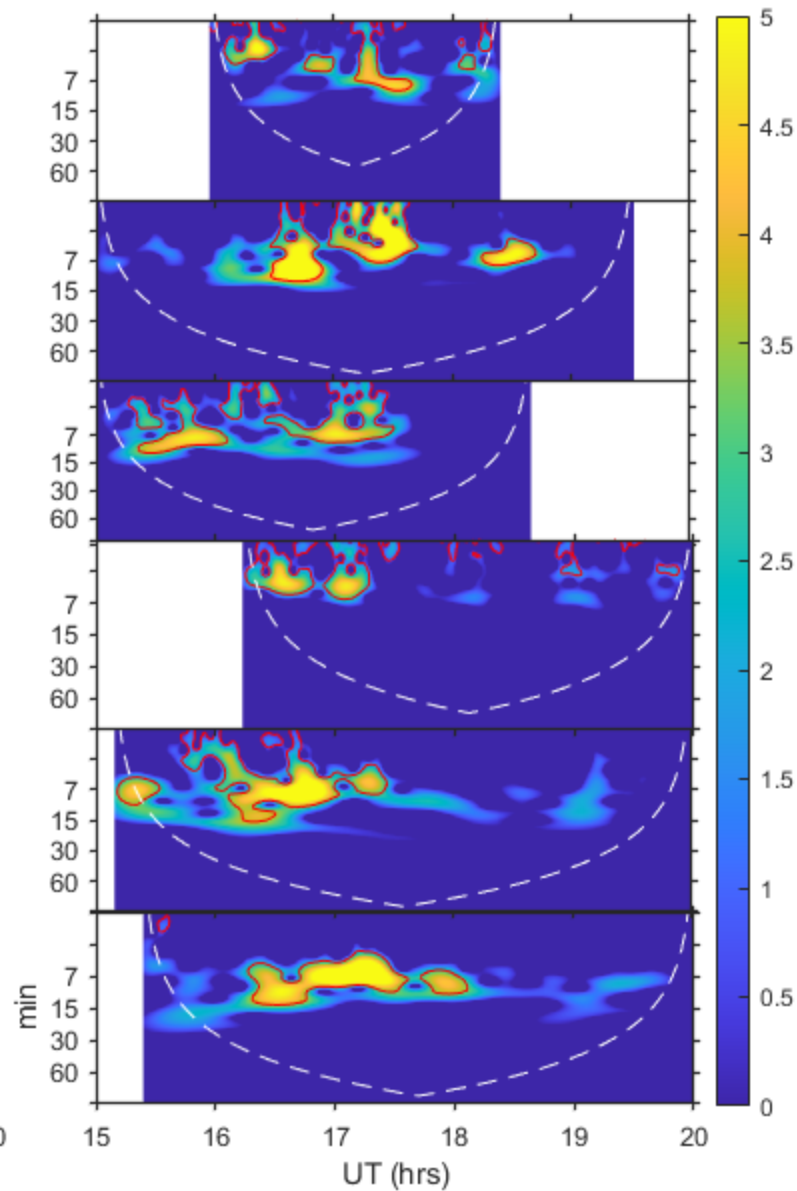


Figure 7.

High Latitude

